



1 **Modelling framework for asynchronous land-atmosphere coupling using**
2 **NASA GISS ModelE and LPJ-LMfire: Design, Application and Evaluation**
3 **for the 2.5ka period**

4

5 Ram Singh^{1,2}, Alexander Koch⁴, Allegra N LeGrande^{2,1}, Kostas Tsigaridis^{1,2}, Riovie D Ramos⁵,
6 Francis Ludlow⁶, Igor Aleinov^{1,2}, Reto Ruedy^{2,3}, Jed O Kaplan⁷

7

8

9 ¹ Center for Climate Systems Research, Columbia University, New York, USA

10 ² NASA Goddard Institute for Space Studies, New York, NY-10025, USA

11 ³ SciSpace LLC, New York, NY, USA

12 ⁴ Department of Earth Sciences, The University of Hong Kong, Hong Kong SAR, China

13 ⁵ Earth Observatory of Singapore, Singapore

14 ⁶ Department of History, School of Histories and Humanities, Trinity College, Dublin 2, Ireland

15 ⁷ Department of Earth, Energy, and Environment, University of Calgary, Calgary AB, Canada

16

17

18 *Correspondence to:* Ram Singh (ram.bhari85@gmail.com)

19



20 **Abstract**

21 While paleoclimate simulations have been a priority for Earth system modelers over the past
22 three decades, little attention has been paid to the period between the mid-Holocene and the Last
23 Millennium, although this is an important period for the emergence of complex societies. Here,
24 we consider the climate of 2500 BP (550 BCE), a period when compared to late preindustrial
25 time, greenhouse gas concentrations were slightly lower, and orbital forcing led to a stronger
26 seasonal cycle in high latitude insolation. To capture the influence of land cover on climate, we
27 asynchronously coupled the NASA GISS ModelE Earth system model with the LPJ-LMfire
28 dynamic global vegetation model. We simulated global climate and assessed our results in the
29 context of independent paleoclimate reconstructions. We also explored a set of combinations of
30 model performance parameters (bias and variability) and demonstrated their importance for the
31 asynchronous coupling framework. The coupled model system shows substantial vegetation
32 albedo feedback to climate. In the absence of a bias correction, while driving LPJ-LMfire in the
33 coupling process, ModelE drifts towards colder conditions in the high latitudes of the Northern
34 Hemisphere in response to land cover simulated by LPJ-LMfire. A regional precipitation
35 response is also prominent in the various combinations of the coupled model system, with a
36 substantial intensification of the Summer Indian Monsoon and a drying pattern over Europe.
37 Evaluation of the simulated climate against reconstructions of temperature from multiple proxies
38 and the isotopic composition of precipitation ($\delta^{18}\text{O}_p$) from speleothems demonstrated the skill of
39 ModelE in simulating past climate. A regional analysis of the simulated vegetation-climate
40 response further confirmed the validity of this approach. The coupled model system is sensitive
41 to the representation of shrubs and this land cover type requires particular attention as a
42 potentially important driver of climate in regions where shrubs are abundant. Our results further
43 demonstrate the importance of bias correction in coupled paleoclimate simulations.



44 1. Introduction

45 Earth system models (ESMs) are widely applied in paleoclimate experiments as an “out of
46 sample” exercise to evaluate the overall quality of the model, and to better understand climate
47 system responses to external forcings. In many paleoclimate modeling studies, it has been
48 demonstrated that inclusion of biogeophysical and biogeochemical feedbacks between land and
49 atmosphere feedbacks are essential to simulate the magnitude and spatial pattern of climate
50 change that is consistent with independent reconstructions (Betts, 2000; Claussen, 1997; Cox et
51 al., 2000; Doherty et al., 2000; Strandberg et al., 2014). The importance of land-atmosphere
52 feedbacks for past climate has shown particularly to be true in the context of the mid-Holocene
53 and last glacial inception periods (Braconnot et al., 2012; Collins et al., 2017; Harrison et al.,
54 2015; Jahn et al., 2005; Kubatzki and Claussen, 1998; Sha et al., 2019; Shanahan et al., 2015;
55 Tierney et al., 2017). For example, for the African Humid Period of the mid-Holocene, numerous
56 studies demonstrated that greenhouse gases (CO₂, N₂O, CH₄) and orbital forcing are alone not
57 sufficient for models to simulate climate that is consistent with independent paleoclimate
58 reconstructions. The inclusion of land-atmosphere feedbacks via interactive dynamic vegetation
59 modeling or prescribed vegetation distributions helps improves model-proxy discrepancies
60 (Chandan and Peltier, 2020; Charney, 1975; Dallmeyer et al., 2021; Pausata et al., 2016;
61 Rachmayani et al., 2015; Singh et al., 2023; Thompson et al., 2021; Tiwari et al., 2023;
62 Velasquez et al., 2021). For this reason, more recent protocols (PMIP4; Otto-Bliesner et al.,
63 2017) for simulations of the mid-Holocene specify that the land cover boundary condition should
64 include shrub vegetation in northern Africa with greater extent than the present (the so-called
65 “Green Sahara”), as well as an expansion of trees and shrubs at high northern latitudes.

66
67 Instead of prescribing land cover boundary conditions in an earth system model, it may be
68 desirable to employ a coupled model where that allows interaction between climate and
69 vegetation. While several modern earth system models include a dynamic representation of land
70 cover, in climate models (regional and global) that lack a coupled dynamic vegetation
71 component a well-established technique to capture land-atmosphere feedbacks is to use
72 asynchronous coupling. In this type of coupling, climate model output is used to drive an offline
73 vegetation model that then returns a land cover boundary condition to the climate model.



74 To quantify the feedback between land and atmosphere and improve the fidelity of the
75 paleoclimate simulation, asynchronous coupling typically involves running a climate model
76 simulation for a period of a few decades, after which the mean climate state is passed to a
77 vegetation model that in-turn produces a land cover boundary condition for the climate model.
78 This process is repeated until climate reaches equilibrium, defined as insignificant changes in
79 key outputs, e.g., 2m temperature, from one cycle to the next.
80

81 Texier et al. (1997) used the iterative asynchronous coupling between the LMD Atmospheric
82 General Circulation Model (AGCM) and the BIOME1 vegetation model to produce an improved
83 climate for the mid-Holocene (6ka) period and found that inclusion of land-atmosphere
84 feedbacks led to simulations of temperatures at high latitudes and precipitation over West Africa
85 that were more consistent with independent paleoclimate reconstructions compared to
86 atmosphere-only simulations. de Noblet et al. (1996) used a similar coupling to highlight the role
87 of biogeophysical feedback in glacial initiation around 115ka ago. Asynchronous coupling has
88 also been used with regional climate models (RCMs). Kjellstrom et al. (2008) and Velasquez et
89 al. (2021) both used asynchronous coupling between an RCM and land cover model to simulate
90 the climate of Europe at the Last Glacial Maximum. Both studies demonstrated the importance
91 of land cover in improving the agreement with reconstructions and paleoenvironmental proxies.
92

93 This study has two objectives. First, we present a generalized design for asynchronously
94 coupling the NASA GISS ModelE2.1 climate model (Kelley et al., 2020) with the LPJ-LMfire
95 DGVM (Pfeiffer et al., 2013) to simulate climate including biogeophysical land-atmosphere
96 feedbacks. Second, we demonstrate the utility of this asynchronous coupling framework for a
97 paleoclimate period that has not been the traditional focus of paleoclimate modeling (2.5 ka) and
98 evaluate the model results against independent paleoclimate reconstructions for that period.
99

100 2.5 ka represents a time that is nearest to the present day among the different periods selected
101 under the coordinated effort of the Paleoclimate Model Intercomparison Project (PMIP4). It is
102 interesting because it represents an important period for the emergence of complex societies
103 across Eurasia (Iron Age, Classical Antiquity, early Imperial China) and elsewhere. During this
104 era, favorable climate conditions around the Mediterranean might have influenced the emergence



105 of the golden age of Greece, the Roman classical period, and other empires of the Southern
106 Europe, North Africa, and southwest Asia (Lamb, 1982; Reale and Dirmeyer, 2000). On the
107 other hand, adverse climate conditions due to volcanic eruptions and a series of arid phases
108 during this period may have had a negative impact on Egyptian civilization around the Nile and
109 Mesopotamian civilization around the Euphrates and Tigris rivers. 2.5ka is thus a key period for
110 the study of human-environment interactions and the history of climate and society, where we
111 may assess societal vulnerability to climate change (Ludlow and Manning, 2021; Manning et al.,
112 2017; Mikhail, 2015; Petit-Maire and Guo, 1998; Singh et al., 2023).

113

114 We evaluate the climate of 2.5 ka simulated with the ModelE-LPJ asynchronous coupling
115 framework against multi-proxy temperature reconstructions (Kaufman et al., 2020) and
116 additionally utilize the model's capabilities to simulate the isotopic composition of water in
117 precipitation ($\delta^{18}\text{O}_p$) to compare with the Speleothem Isotope Synthesis and Analysis (SISAL)
118 version 2 database (Comas-Bru et al., 2020).

119

120 **2. Models and Methodology**

121 **2.1.1 NASA GISS ModelE2.1:** NASA GISS ModelE2.1 (Kelley et al., 2020), is the climate model
122 of the NASA Goddard Institute for Space Studies (GISS) currently used in Climate Model
123 Intercomparison Project (CMIP) phase 6 (Eyring et al., 2016). We used the NINT (Non-
124 Interactive; physics version 1 in CMIP6) GISS ModelE2.1 version where aerosols and ozone are
125 precomputed from the prognostic, but much more computationally demanding, chemistry and
126 aerosols version of the model OMA (One Moment Aerosols; physics version 3 in CMIP6; (Bauer
127 et al., 2020)). In our simulations, the GISS ModelE2.1 atmosphere has a horizontal resolution of
128 $2^\circ \times 2.5^\circ$ (latitude/longitude) with 40 vertical layers, and the top of the atmosphere at 0.1 hPa. The
129 ModelE2.1 atmosphere has a smooth transition from sigma layers to constant pressure layers
130 centered at 100hPa. The atmosphere is coupled to the GISS Ocean v1 model, which runs at a
131 resolution of $1^\circ \times 1.25^\circ$ (latitude/longitude) with 40 depth layers to the ocean bottom. While the
132 biogeophysical properties of land cover are simulated with the Ent Terrestrial Biosphere Model
133 (Ent TBM; Kiang 2012; (Kim et al., 2015)), as part of ModelE2.1 (Ito et al., 2020), Ent relies on
134 a prescribed vegetation map and as such does not simulate changes in land cover over time. To
135 capture the influence of climate change on land cover and biogeophysical feedbacks between land



136 and atmosphere, asynchronous coupling with LPJ-LMfire (or any other DGVM) is currently
137 required.

138

139 **2.1.2 LPJ-LMfire:** We used the LPJ-LMfire DGVM (v1.4.0) to simulate the land cover
140 boundary conditions in our experiments. LPJ-LMfire (Kaplan et al., 2022; Pfeiffer et al., 2013) is
141 an evolution of LPJ (Sitch et al., 2003) and is a process-based, large-scale representation of plant
142 growth and decay, vegetation demographics and ecological disturbance, and water and carbon
143 exchanges between the land and the atmosphere. For this study, we simulated land cover
144 boundary conditions at a horizontal resolution $0.5^\circ \times 0.5^\circ$. LPJ-LMfire is driven by monthly fields
145 of climate (temperature, precipitation, cloud cover, wind, and lightning), static maps of
146 topography and soil texture, and an annual global value of atmospheric CO_2 concentration. LPJ-
147 LMfire simulates land cover in the form of fractional coverages of nine plant functional types
148 (PFTs), including tropical, temperate, and boreal trees, and tropical and extratropical herbaceous
149 vegetation (Table 1). CO_2 , soil texture and topography data used to drive LPJ-LMfire are
150 described in Pfeiffer et al. (2013, Table 3). For 2.5ka simulations, we set atmospheric CO_2
151 concentrations to 271.4 ppm (Krumhardt and Kaplan, 2012). The sum of PFT fractional cover
152 per grid box does not need to equal unity; when it is less than one the remainder is considered
153 bare ground.

154



155

GISS Output	LPJ -LMfire Input		LPJ-LMfire Output Vegetation (PFTs)		GISS ModelE (Ent) Vegetation (PFTs)
Surface Air Temperature	Surface Air Temperature	Annual cycle climatology and variability (standard deviation) over the period of interest (100 Years)	Tropical Broadleaf Evergreen	LPJ-LMfire to GISS ModelE (Ent) Vegetation Mapping (Vegetation cover type, Leaf area index and vegetation heights)	Evergreen Broadleaf Late Succession
Precipitation	Precipitation		Tropical Broadleaf Raingreen		Evergreen Broadleaf Late Succession
	Number of wet days		Temperate Needleleaf Evergreen		Cold Deciduous Broadleaf Late Succession
Diurnal Surf. Air Temp Range	Diurnal Surf. Air Temp Range		Temperate Broadleaf Evergreen		Drought Deciduous Broadleaf
Surface Wind Speed	Surface Wind Speed		Temperate Broadleaf Summergreen		Deciduous Needleleaf
Moist Convective Air Mass Flux	Lightning Density		Boreal Needleleaf Evergreen		Cold Adapted Shrub
			Boreal Summergreen		Arid Adapted Shrub
			C3 Perennial Grass		C3 Grass Perennial
			C4 Perennial Grass		C4 Grass
					C3 Grass Annual
			Arctic C3 Grass		
			Bright Bare Soil		
			Dark Bare Soil		

156



157 **Table 1:** - Summary of climate and PFT variables exchanged between NASA GISS ModelE and
158 LPJ-LMFire model for asynchronous coupling process. Column 1 and 2 shows lists the output and
159 input climate variables from GISS ModelE to LPJ-LMFire models, whereas the columns 3 and 4
160 lists the output and input plant function types (PFTs) from LPJ-Lmfire to GISS ModelE.

161

162 **2.2. 2.5ka Simulation setup (ModelE)**

163 We started the 2.5ka and preindustrial (PI) control experiments following the PMIP4 and CMIP6
164 protocols (Eyring et al., 2016; Kageyama et al., 2018). The PI simulation uses preindustrial (year
165 1850) GHG concentrations and a modern continental configuration and serves as the reference
166 experiment for designing the boundary conditions for past time slices studied in PMIP4. GHG and
167 orbital forcings for the preindustrial (PI) control experiment correspond to levels observed in
168 1850 CE (CO₂: 284 ppm, N₂O: 273 ppb, CH₄: 808 ppb). For the 2.5 ka control experiment, orbital
169 parameters (Berger et al., 2006) were specified for 2,500 years BP (~550 BCE), and greenhouse
170 gas CO₂, N₂O, and CH₄ were set to ~279 ppm, ~266 ppb, and 610 ppb respectively (Loulergue et
171 al., 2008; Otto-Bliesner et al., 2017; Schneider et al., 2013; Siegenthaler et al., 2005). We
172 considered only natural emissions as sources of aerosols in the atmosphere, zeroing-out any
173 anthropogenic contribution to aerosol and aerosol precursors. For biomass burning, in the absence
174 of any better estimate, we assumed that the emissions provided by CEDS (Hoesly et al., 2018) for
175 the year 1750 are all natural. Land cover consists of the fractional coverages of 13 plant functional
176 types (PFTs) and includes vegetation height and leaf area index (LAI). For the PI and initial (0th
177 order) simulations, land cover type and monthly-varying LAI were derived from satellite (MODIS)
178 data (Gao et al., 2008; Kattge et al., 2011; Myneni et al., 2002; Tian et al., 2002a, b; Yang et al.,
179 2006) and vegetation heights from (Simard et al., 2011). We also used the mid-Holocene (6k)
180 vegetation under PMIP4 protocol, which is linearly interpolated to 2.5ka period and details of
181 vegetation cover changes (Singh et al., 2023; Figure S1) and associated impacts on the northern
182 hemisphere climate due to the inclusion of scaled PMIP4 vegetation using the interactive chemistry
183 version of NASA GISS ModelE2.1 (MATRIX) are discussed in (Singh et al., 2023).

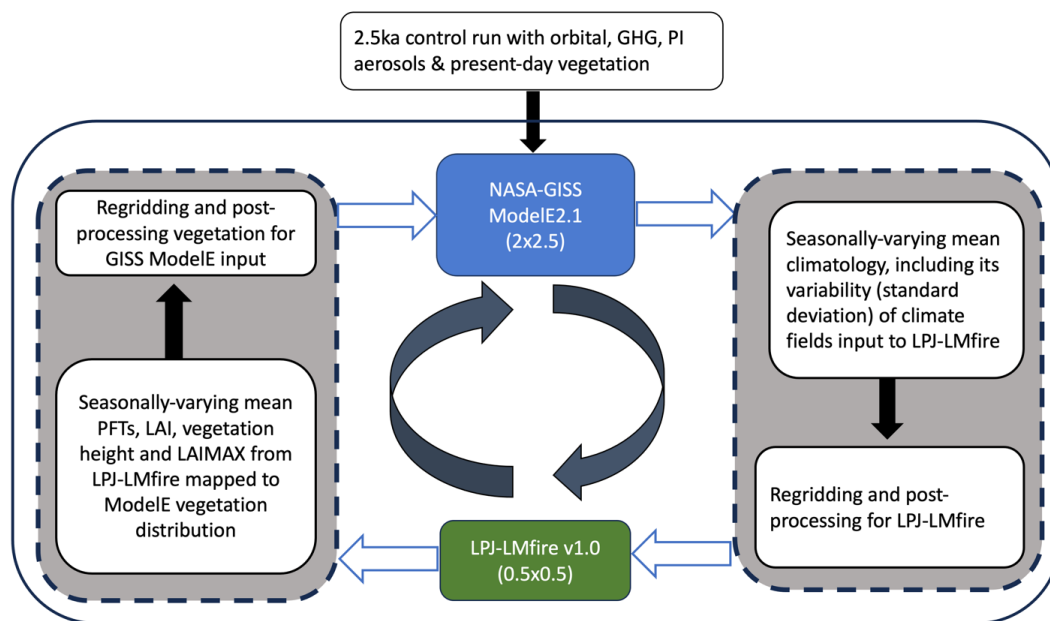
184

185 **2.3 Asynchronous Coupling Framework**

186 The asynchronous coupling between ModelE and LPJ-LMfire is summarized in Figure 1. For each
187 iteration, ModelE simulated climate is used by LPJ-LMfire, which, returns the PFT fractional



188 cover, LAI, and vegetation height that are used as boundary conditions for the next ModelE
189 simulation.



190
191

192 Figure 1: Flow diagram for the asynchronous coupling between GISS ModelE2.1 and LPJ-LMfire
193 models. For the climate fields input to LPJ-LMfire refer to (Table 1, Column 1) and LPJ-LMfire
194 PFTs (Table 1, Column 3)

195

196 **2.3.1 GISS ModelE2.1 simulations:** Climatological monthly mean climate (Table 1, Column 1)
197 for a 100-year period were extracted from a well equilibrated ModelE simulation. To assess
198 interannual variability with monthly resolution, we calculated the standard deviation of the decadal
199 mean data for each month across the 100-year equilibrium period.

200 **2.3.2. LPJ-LMfire simulations:** All climate variables except diurnal temperature range, wet days,
201 and lightning density were provided directly from the ModelE output. For derived climate
202 variables, the additional processing steps are described below.

203

204 Diurnal temperature range was calculated as the difference of the monthly-mean daily maximum
205 and minimum temperatures as simulated by ModelE. Wet days were calculated from modelled
206 precipitation based on an empirical relationship between present-day monthly total precipitation



207 and the number of wet days per month. To quantify this relationship, we performed a nonlinear
208 regression between monthly total precipitation and number of days with measurable precipitation
209 using the CRU TS 4.0 gridded climate fields (Harris et al., 2020). Using those data, we developed
210 a set of regression coefficients for every land gridcell that allowed us to estimate wet days for any
211 paleoclimate period based only on monthly total precipitation. Lightning density was estimated
212 based on modelled convective mass flux following Magi (2015).

213

214 Because LPJ-LMfire requires a timeseries of interannually varying climate forcing to run, we
215 processed the climatological monthly mean climate produced by the ModelE for use with the
216 vegetation model. In brief, ModelE climate was converted into anomalies by differencing the
217 paleoclimate simulation with ModelE simulated climate for the late 20th century (1951-2000). The
218 resulting climate anomalies were linearly interpolated to a 0.5°x0.5° grid and added to a baseline
219 climate based on observations over 1951-2000. The resulting climatology was expanded to a 1020-
220 year-long time series by adding interannual variability in the form of detrended and randomized
221 climate anomalies from the 20th Century Reanalysis (Compo et al., 2011). For further details on
222 this process, see (Hamilton et al., 2018). Because LPJ-LMfire is computationally inexpensive, we
223 ran each simulation for 1020 years. While the composition and characteristics of aboveground
224 vegetation comes into equilibrium with climate after a few centuries of simulation, a millennium-
225 long simulation brings the terrestrial carbon pools into equilibrium as well. The land cover
226 boundary conditions returned to the climate model represent the mean modeled vegetation cover
227 over the final 250 years of the LPJ-LMfire simulation.

228

229 **2.3.3. LPJ-LMfire to GISS ModelE vegetation mapping:** LPJ-LMfire simulates land cover in
230 the form of nine PFTs, while in GISS ModelE the vegetation component (Ent TBM) recognizes
231 13 PFTs. We mapped the LPJ-LMfire generated PFT cover, LAI, LAIMAX, and vegetation height
232 to the GISS ModelE2.1 (Ent) PFTs in order to feed it to the ModelE (Table 1, Column 3 & 4). The
233 main points for the LPJ-LMfire to GISS vegetation mapping are the following:

234

235 - Early and late-successional PFTs were approximated from the LPJ-LMfire output using
236 the model simulated fire frequency and monthly burned area fraction. However, because
237 successional state is indistinguishable in the satellite-driven reference vegetation for the



238 historical period used as the boundary condition for ModelE, we combined early & late
239 successional PFTs in our simulations.

240 - LPJ-LMfire does not have a specific PFT for shrubs (arid and cold), while Ent does. To
241 estimate shrub cover in LPJ-LMfire, we used LPJ-LMfire simulated tree height for the
242 tropical broadleaf raingreen, temperate broadleaf summergreen, and boreal summergreen
243 PFTs and specified that trees with height lower than a predefined threshold were considered
244 to be shrubs (Table S1).

245 - Ent has an Arctic grass PFT while LPJ-LMfire does not. To estimate Arctic grass cover we
246 used the C₃ grass PFT in LPJ-LMfire and specified it as Arctic grass in regions where the
247 boreal summergreen PFT was also present. LPJ-LMfire also does not distinguish between
248 annual and perennial grasses, and so to map these to Ent we assumed that these were
249 present in equal fractions among the simulated C₃ grass in the LPJ-LMfire simulation.

250 - The non-vegetated fraction of a grid cell is assigned to the bare soil, and the distribution of
251 bright and dark soil color heterogeneity is classified/redistributed based on the present-day
252 structure of soils over a grid cell.

253

254 Of particular importance to our coupled model simulations was that the PFTs simulated by LPJ-
255 LMfire do not explicitly include a shrub type. To approximately distinguish tree from shrub cover,
256 we generated three LPJ-to-GISS mapping schemes that differed on how shrubs are specified. A
257 set of possible changes in various PFT classifications are adopted based on the comparison with
258 GISS vegetation distribution and categorized the mapping methodologies. These mappings,
259 summarized in table S1, differ in the height threshold of trees to be re-categorized as cold and arid
260 shrubs, and the fraction of perennial grass re-categorized into perennial and arctic grasses. Also,
261 the monthly leaf area index (LAI) and vegetation height readjusted using the weighted mean for
262 remapped LPJ-LMfire vegetation PFTs.

263

264 **2.3.4. Step 4. Post-processing of vegetation files:** LPJ-LMfire model generates output at a
265 horizontal resolution of 0.5°x0.5°. We resampled the output vegetation information to the
266 2.0°x2.5° grid used by ModelE2.1. In a few cases, land cover extrapolated using a nearest-neighbor
267 approach was to cover all the gridcells identified as land in the ModelE standard land-sea mask.

268



269 3 Experimental Design

270 Apart from evaluating the framework for the PI control period, we designed a set of experiments
271 to evaluate various aspects of the simulated climate, including model bias, and variability in both
272 the climate vegetation models. For example, one known limitation in the current version of
273 ModelE is a wintertime cold bias over the Arctic in simulations covering the historical period
274 (Kelley et al., 2020).

275

276 Table 2 shows the combinations of the model metrics selected to explore the utility of the
277 asynchronous coupling framework and their impact on simulated climate. Run names are
278 designated using Time (1850, 2.5k), Vegetation source (PI, GS), Bias Correction (BC) and
279 Interannual Variability (LPJ, GISS) separated by “_”. For example, ‘1850_PI_ctrl’ and
280 ‘2.5k_PI_ctrl’ denote the 1000-year-long PI and 2.5k runs with GISS PI vegetation. GS stands for
281 Green Sahara and PI = Pre-Industrial. An “x” denotes the absence of a particular criterion (default
282 state). Runs ‘2.5k_PI_BC_LPJ’, ‘2.5k_PI_x_x’, and ‘2.5k_PI_x_GISS’ are three branches
283 extended from ‘2.5k_PI_ctrl’ with the combinations of bias correction and interannual variability
284 from LPJ and GISS models. For the ‘2.5k_GS_x_GISS’ and ‘2.5k_GS_BC_GISS’ simulations,
285 we initialized the land cover boundary conditions to approximate 2.5 ka by linearly interpolating
286 cover fractions between the 6 ka land cover prescribed under the PMIP4 protocol (Otto-Bliesner
287 et al., 2017) and the PI reference dataset. Details of the 6 ka land cover boundary conditions under
288 for PMIP4 and associated impacts on Northern Hemisphere climate using the interactive chemistry
289 version of NASA GISS ModelE2.1 (MATRIX) are discussed by (Singh et al., 2023).

290



291 **Table 2:** - Summary of experiment designs followed to explore and evaluate the GISS ModelE -
 292 LPJ-LMFire model asynchronous coupling framework. See text for an explanation on the run
 293 naming convention.

Run Name	Initial Vegetation Cover	Bias correction	Interannual Variability	Number of Iterations/total number of years	Remark
1850_PI_ctrl	Used to evaluate the LPJ to GISS vegetation mapping schemes				
2.5k_PI_ctrl	1000-year-long control; base run to branch out the other simulations				
2.5k_PI_BC_LPJ	GISS PI vegetation	YES	LPJ	5/750 years	converged
2.5k_PI_x_x	GISS PI vegetation	No	No	2/270 years	Too cold in 3 rd iteration diverging
2.5k_PI_x_GISS	GISS PI vegetation	No	GISS ModelE (100years)	4/550 years	Too cold diverging
2.5k_GS_x_GISS	GISS PI vegetation + Green Sahara+ Boreal Forest	No	GISS ModelE (100years)	5/1150 years	Too cold diverging
2.5k_GS_BC_GISS	GISS PI vegetation + Green Sahara+ Boreal Forest	YES	GISS ModelE (100years)	4/1000 years	converged

294 * Convergence means the final model simulation has a similar climatology with the previous
 295 iteration, whereas divergence means the model is drifting away from the expected states.

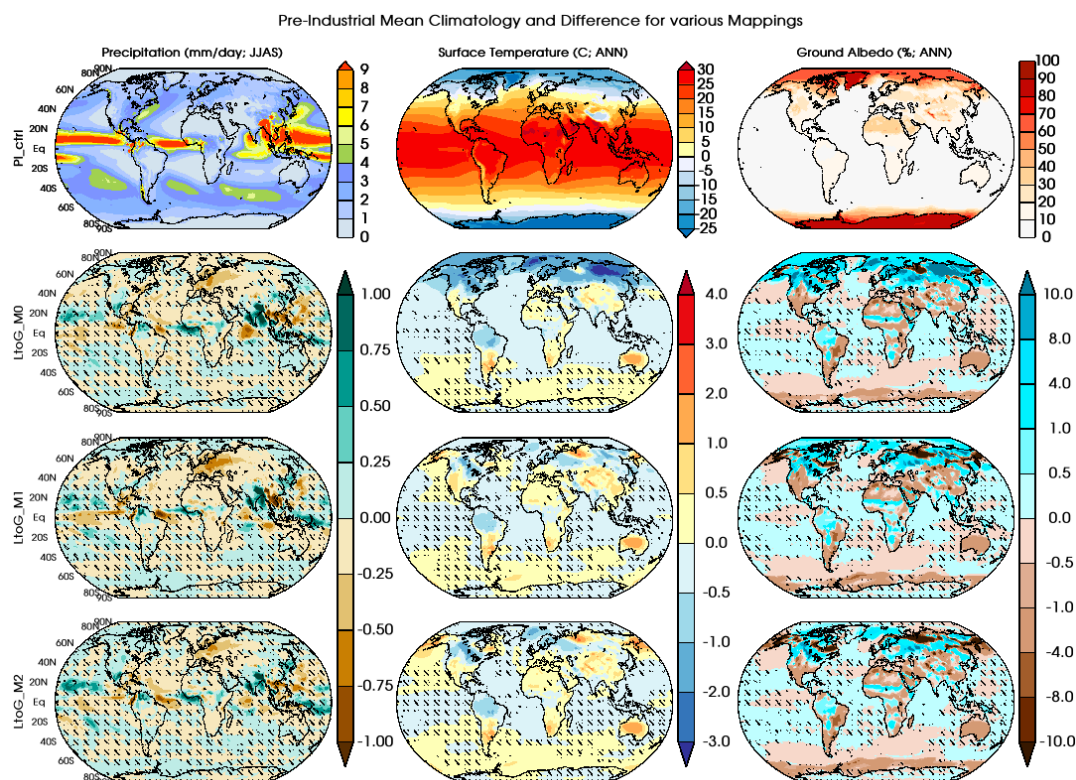
296
 297



298 **3.1 Evaluation & Validation of LPJ-GISS Mapping Methodologies**

299 We used the standard present-day land cover boundary conditions described for ModelE2.1
300 (Kelley et al., 2020) for the initial 0th-order iteration of the pre-industrial and 2.5ka control
301 climate simulations. This land cover dataset is based on satellite observations (Gao et al., 2008;
302 Myneni et al., 2002; Tian et al., 2002a, 2002b; Yang et al., 2006) from the Moderate Resolution
303 Imaging Spectroradiometer (MODIS), with leaf area index (LAI) from the TRY database (Kattge
304 et al. 2011), and vegetation height (Simard et al. 2011) from the Geoscience Laser Altimeter
305 System (GLAS). Branches of the 2.5ka run for green Sahara conditions are started using the
306 linearly interpolated vegetations for 2.5ka from the 6ka vegetation distribution defined based on
307 the PMIP4 protocol (Otto-Bliesner et al., 2017; Singh et al., 2023). These land cover boundary
308 conditions are shown as the fractional coverage of 13 PFTs (including bare soils) (Figs. S1.A and
309 S1.B). In these figures, bare dark and bare bright are merged into a single bare soil fractional
310 cover.

311
312 The ModelE2.1 pre-industrial (PI) control run initialized with the present-day land cover boundary
313 condition is processed through the asynchronous coupling framework to evaluate the mapping
314 scheme for converting LPJ PFTs to GISS (Ent) PFTs. We tested three sets of LPJ-to-GISS
315 mapping schemes as required in the asynchronous coupling framework. Differences among the
316 mapping schemes are described in supplementary table TS1. Three parallel control runs are
317 performed for 100 years, each initialized with the vegetation distribution that corresponds to the
318 corresponding mapping scheme and compared to the mean climate state of the parent PI control
319 run.
320



321
322 **Figure 2.** Comparison of seasonal mean climate metrics when using different vegetation mapping
323 schemes with that of the origin PI control. Top row shows the mean climatology for precipitation
324 (mm/day; JJAS), surface air temperature (°C; ANN) and ground albedo (%; ANN) and row 2 to 4
325 differences in mean climate for LtoG_M0, LtoG_M1 and LtoG_M2, respectively.

326
327 The mapping schemes LtoG_M1 and LtoG_M2 (supplementary table TS1) generate a similar
328 spatial structure of annual surface air temperature with broadly similar regional characteristics
329 (Fig. 2). A shift towards colder climates of 2-3 °C in mean annual temperature over the higher
330 latitudes of the Northern hemisphere is simulated when using the mapping scheme LtoG_M0,
331 which is not present when using the other mapping schemes (LtoG_M1 and LtoG_M2). We
332 selected forests into shrubs to match the missing PFTs in ModelE vegetation distributions based
333 upon the tree height (Table S1). In these mapping schemes, the fraction of boreal tree PFTs
334 assigned to cold shrubs depends on simulated tree height, which is, in turn, influenced by surface
335 temperature (Thomas and Rowntree, 1992; Bonan et al., 1992; 2008; Li et al., 2013). In the



336 mapping LtoG_M0, the fractional cover of boreal tree PFTs was reduced significantly, leading to
337 an increase in ground albedo (up to 10%), which led to the model drifting towards comparatively
338 colder climate conditions. When using the other two mapping schemes (LtoG_M1 and
339 LtoG_M2) the assignment of boreal tree PFTs to shrub types is limited by a higher tree height
340 threshold and partially because other PFTs (perennial grass) are substituted for cold shrubs.
341 Regional patches of increased ground albedo and surface cooling over the higher latitudes of the
342 Northern Hemisphere are also evident when using the LtoG_M1 and LtoG_M2 translation
343 schemes.

344

345 Precipitation during the Northern Hemisphere summer monsoon season (JJAS; June-July-
346 August-September) appears similar among the three mapping schemes, as the larger changes are
347 confined to the equatorial regions. A drying pattern over Europe appears in all three translation
348 schemes, but it is comparatively more substantial under LtoG_M0 and LtoG_M1 than LtoG_M2.

349

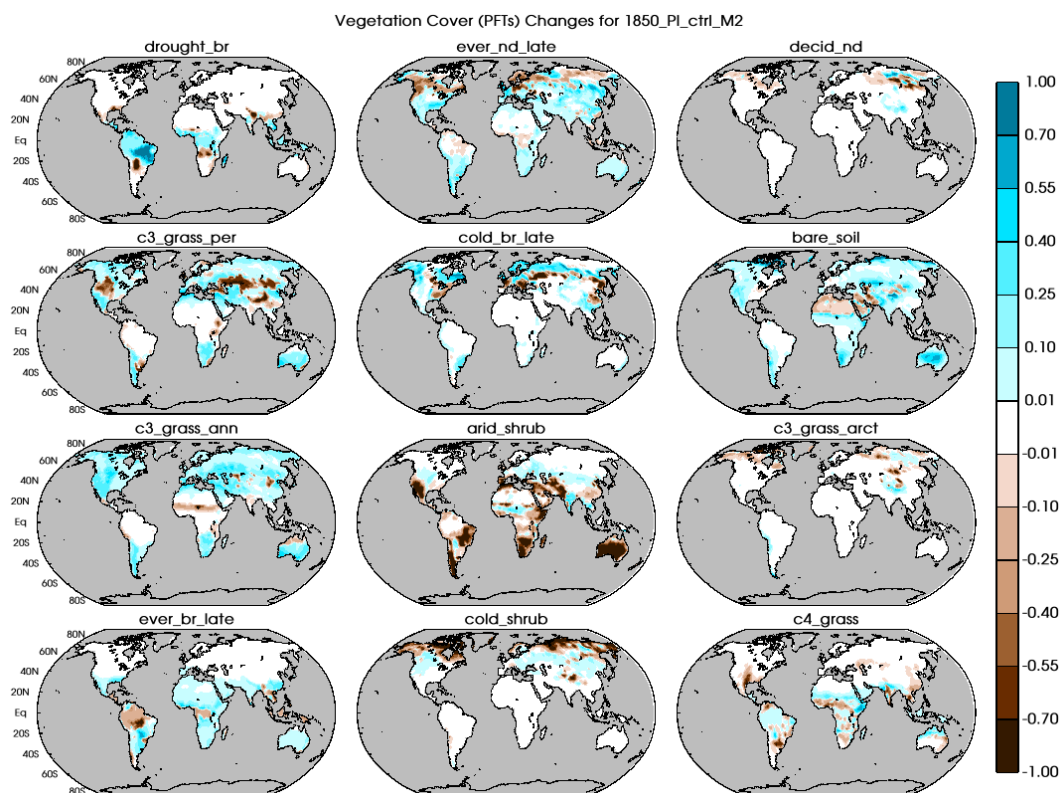
350 All translation schemes also lead to increased precipitation over equatorial South America.
351 Annual mean river runoff for the Amazon River is simulated at 305, 297, and 308 km³/month for
352 LtoG_M0, LtoG_M1 and LtoG_M2, respectively, a slight improvement to the original
353 Preindustrial (PI) run runoff of 280 km³/month with using the standard present-day land cover
354 boundary condition. Compared to observations, ModelE2.1 shows a substantial deficit in
355 Amazon River runoff in present-day simulations because of insufficient precipitation over the
356 watershed (Fekete et al., 2001; Kelley et al., 2020).

357

358 Based on this evaluation of the different ways of translating LPJ PFTs to GISS PFTs, we found
359 that LtoG_M2 was the scheme that simulates global precipitation and surface temperature most
360 consistent with observations, and ground albedo that is closest to the standard pre-industrial
361 boundary conditions dataset used usually used to drive ModelE. Figure 3 shows the difference in
362 PFT cover fraction using LPJ-LMfire with the LtoG_M2 scheme compared to the standard
363 ModelE boundary condition land cover data set for the late preindustrial time (PI; 1850 CE).
364 Compared to the ModelE standard land cover dataset for PI, LPJ-LMfire simulates increased
365 extent and fraction of most trees (drought broadleaf, evergreen needleleaf, and evergreen
366 broadleaf). Despite selecting a relatively high threshold for tree height to be classified as shrubs



367 (up to 11 meters for both arid and cold types) the simulated cover fraction of shrubs is low
368 compared to the standard PI land cover dataset for ModelE. The coverage of both annual and
369 perennial C₃ grasses is greater in LPJ-LMfire in extratropical and polar regions, similarly, C₄
370 grasses, which are not present in cooler climates, shows greater coverage in LPJ-LMfire in
371 equatorial regions. LPJ-LMfire simulates some vegetation cover in the Sahara and Arabian
372 deserts while the standard PI boundary conditions dataset suggests that most of this region is
373 bare soil.
374



375
376 **Figure 3.** Differences between the LPJ-LMfire simulated vegetation distribution (PFTs and land
377 cover type) and satellite-based land cover boundary conditions used in ModelE for PI control
378 period under the selected mapping schemes (LtoG_M2).

379

380 3.3 Vegetation Cover Changes under various combinations



381 We chose a set of five model configurations (Table 2) to quantify the model bias and interannual
382 variability in our asynchronous coupling framework for the 2.5ka period. Figures S2.A, S2.B,
383 S2.C, S2D, and S2.E show the spatial differences between prescribed land cover boundary
384 conditions maps and land cover interactively simulated by our LPJ-LMfire-ModelE coupled
385 model, which is henceforth referred to as the “coupled model system”. These land cover
386 difference maps are shown for each of the different model configurations described above,
387 following the final iteration of the asynchronous coupling when the coupled model system is
388 assumed to be either equilibrated or the process was truncated due to instability (Table 2).
389 Figures S2.A, S2.B, and S2.C show the changes in the land cover from the default ModelE land
390 cover boundary conditions map for PI (Fig S1.A); Figures S2.D and S2.E show the differences
391 calculated from the modified vegetation following the PMIP4 protocols (Fig S1.B).

392

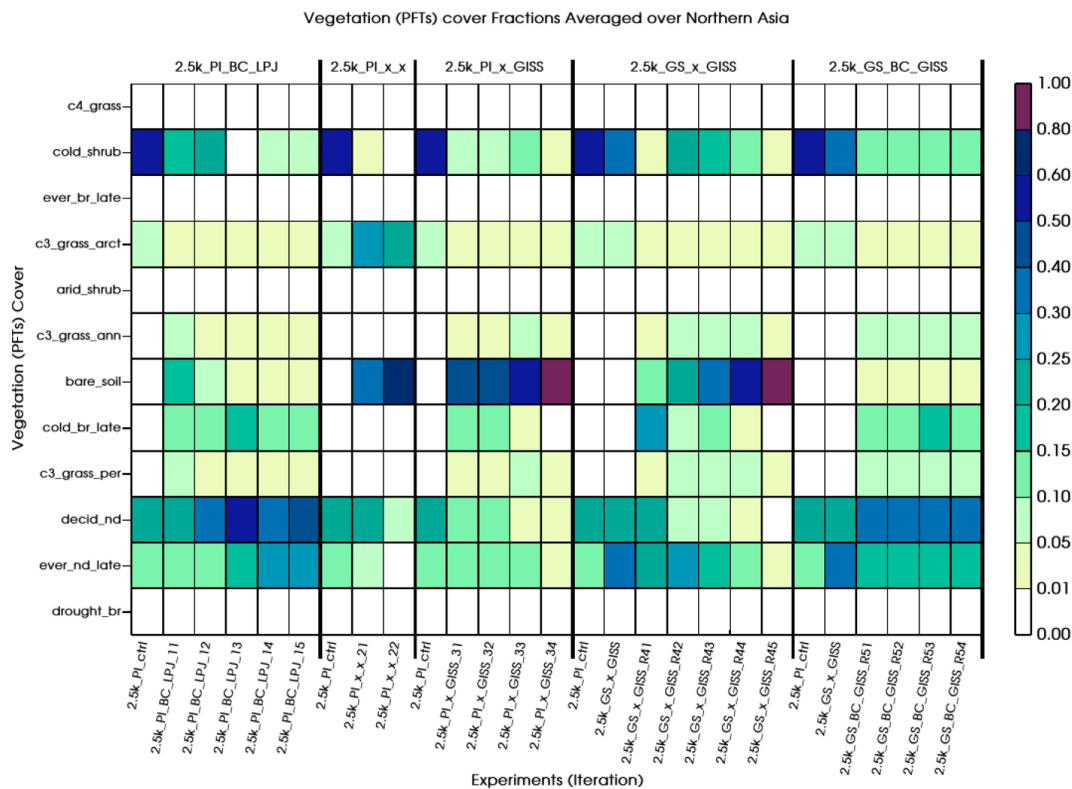
393 Across all configurations, most of the tree PFTs show an increase in cover in the coupled model
394 system relative to the prescribed land cover maps. However, in simulations where bias correction
395 to the climate model was not applied, deciduous needleleaf tree cover is reduced in the high
396 latitudes of the Northern Hemisphere (2.5k_PI_x_x, 2.5k_PI_x_GISS and 2.5k_GS_x_GISS)
397 and this, in turn, has a substantial impact on regional climate. The coupled model system
398 simulates increased annual and perennial C₃ grass cover across all configurations relative to the
399 prescribed maps, while the Arctic C₃ grass shows a mixed regional response. Increased C₄ grass
400 cover is mostly confined to the equatorial region and Southern Hemisphere; over the Northern
401 Hemisphere C₄ grass cover decreases, irrespective of the inclusion and exclusion of interannual
402 variability or bias correction. As discussed previously, the extent of arid and cold shrubs is
403 reduced significantly in the coupled model system relative to the prescribed maps, even when the
404 threshold height to separate trees shrubs was set at a relatively tall limit of 11 m. A similar
405 reduction in shrub cover relative to the land cover map used to initialize the simulation
406 vegetation distributions is also simulated under all configurations.

407

408 In Figures 4 and 5 we present heatmap-type diagrams of the mean land cover fraction over
409 selected regions to demonstrate and understand the pattern of change in vegetation distribution
410 simulated by the coupled model system. These figures depict changes in land cover under the
411 different asynchronous coupling experimental configurations used in this study. Vegetation



412 fraction changes averaged over northern Asia (NAS) (Fig. 4) and eastern Africa (Fig. 5; see Fig.
 413 9 for the region boundaries; NAS: magenta; EAF: blue). Deciduous needleleaf tree cover over
 414 northern Asia (60°N-77°N, 70°E-135°E) is replaced by bare soil in all experimental
 415 configurations where bias correction of the climate model output was not applied. A similar
 416 disappearance of evergreen needleleaf late-successional forests, as well as a quick disappearance
 417 (within the first iteration) of cold shrubs, was also noticed. This suggests that, in the absence of
 418 bias correction the model's drift towards colder conditions strongly influences vegetation growth
 419 in subsequent iterations over higher latitudes, which is inconsistent with the standard land cover
 420 boundary condition dataset used with ModelE (Kelley et al., 2020). On the other hand, when bias
 421 correction is applied along with interannual variability from either model (2.5K_PI_BC_LPJ and
 422 2.5K_GS_BC_GISS), boreal forests are present in the northern Asia region along with cold
 423 shrubs and grasses.
 424



425

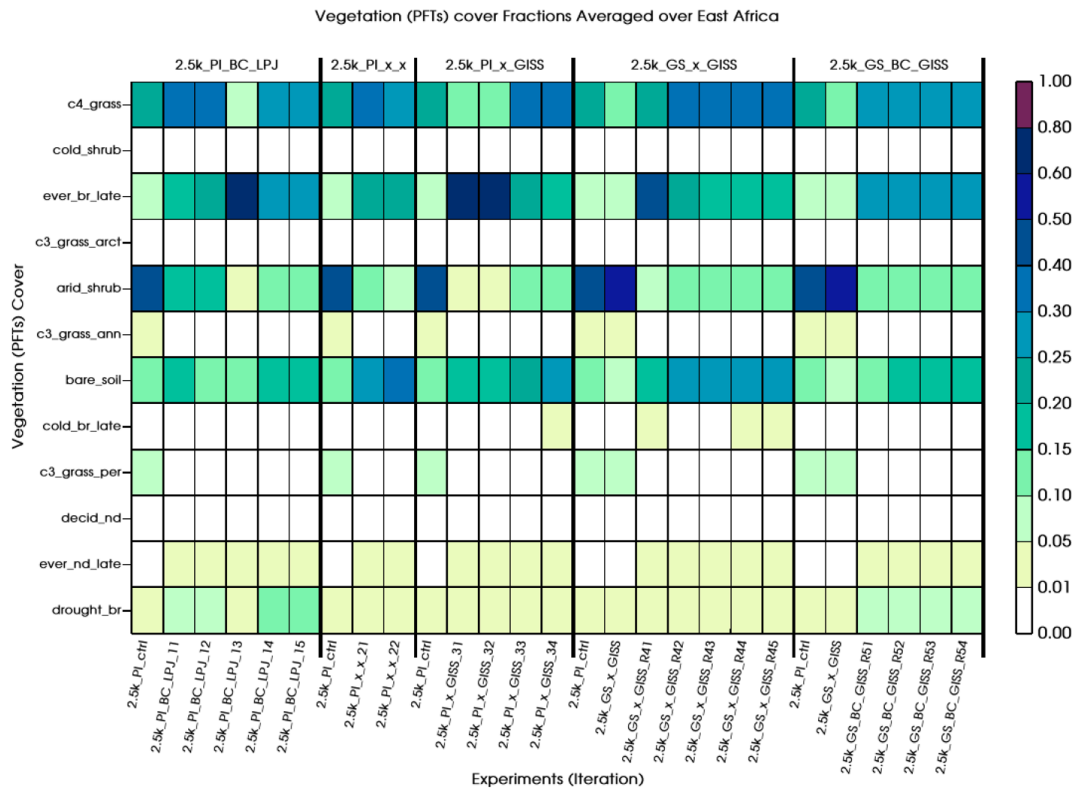


426 Figure 4. Area average of fractional land cover over Northern Asia (60°N-77°N, 70°E-135°E)
 427 under the range of experimental configurations used in this study.

428

429 Over eastern Africa (EAF: 0° N-18° N, 25° E-46° E) the impact of bias correction is less
 430 important than over the high latitudes of the Northern Hemisphere. The presence of broadleaf
 431 tree PFTs (drought broadleaf and evergreen broadleaf) and C₄ grasses is consistent across all the
 432 experimental configurations we used. However, the cover fraction arid shrubs decreased
 433 substantially, associated with a slight increase in the bare soil fraction.

434



435

436 Figure 5. Same as Figure 4A, but for eastern Africa (0°N-18°N, 25°E-46°E).

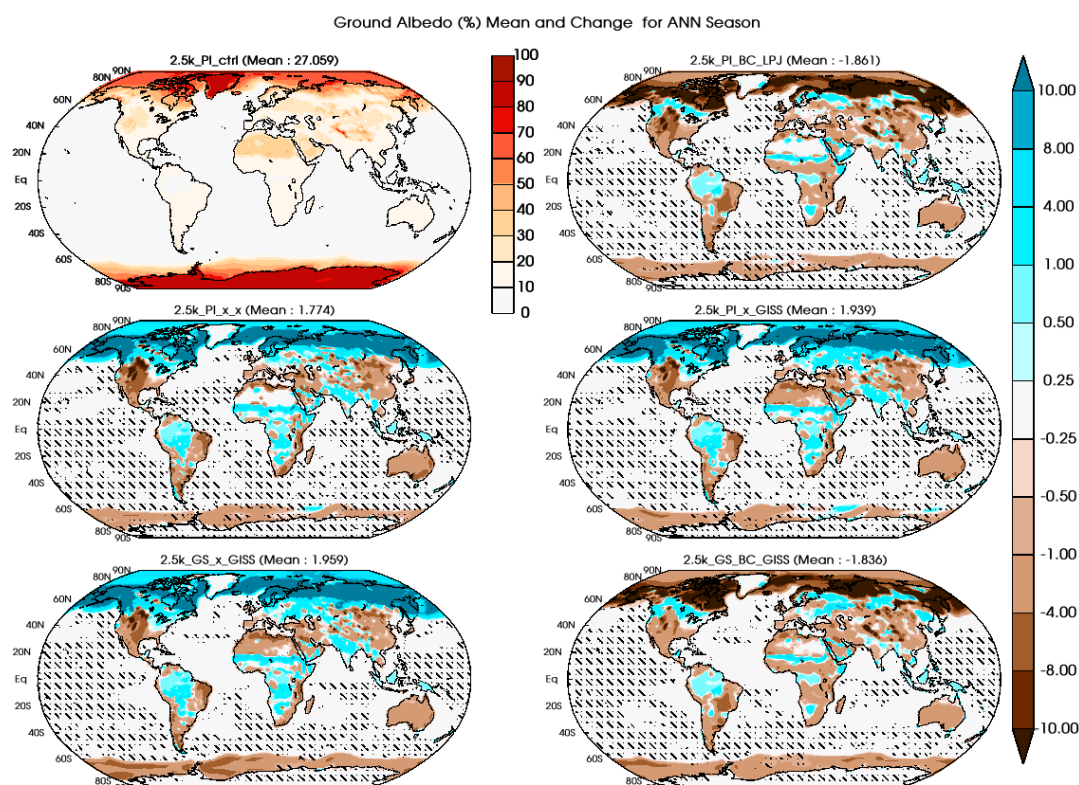
437

438 4. Global climate response

439 To evaluate the spatial features of the equilibrium climate simulated by ModelE, we analyzed the
 440 last 100 years of the final iteration of each coupled model system experimental configuration. We



441 aimed to understand the biogeophysical feedback due to vegetation cover changes as well as the
442 role of model configuration on climate. Figure 6 shows surface albedo (%) for ModelE in its initial
443 PI state, and differences between this initial state and simulated albedo for 2.5ka using the coupled
444 model system. We used student's t-tests to estimate if the albedo differences were statistically
445 significant at 95% confidence interval. The coupled model system shows substantial vegetation
446 cover change over the high latitudes of the Northern Hemisphere. As expected, most of the
447 significant changes occur over land, while changes in albedo over the oceans are largely
448 insignificant. The spatial pattern of albedo change differs between simulations where bias
449 correction was applied (2.5k_PI_BC_LPJ and 2.5k_GS_BC_GISS) and those where it was not
450 (2.5k_PI_x_x, 2.5k_PI_x_GISS, and 2.5k_GS_x_GISS). Albedo over the high latitudes of the
451 Northern Hemisphere decreases up to 10% caused by increased tree cover fraction (deciduous
452 needleleaf and evergreen needleleaf) in the coupled model system relative to standard PI land
453 cover dataset.
454



455



456 Figure 6. Annual mean (top left; 2.5k_PI_ctrl) and change (all other panels) of surface albedo (%)
457 for the various configurations listed in Table 2. Stippling indicates the region over which change
458 is statistically insignificant at a 95% confidence interval (student's t-test).

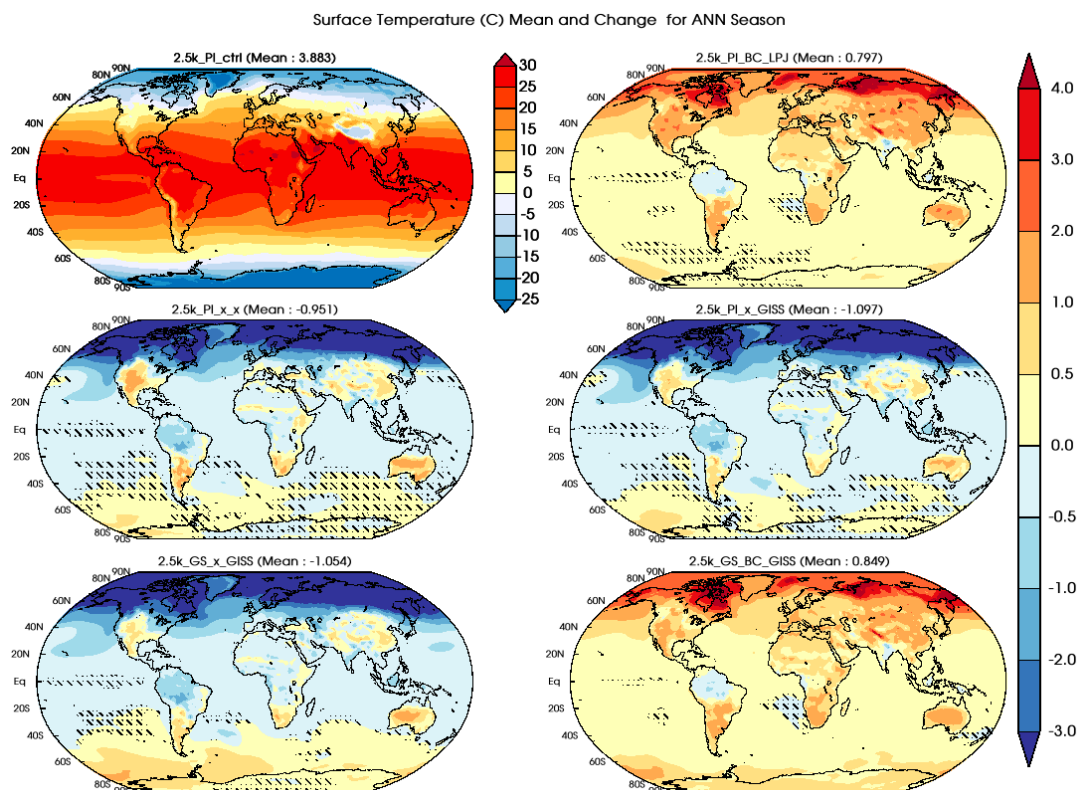
459

460 This increased tree cover fraction subsequently absorbs more incoming solar radiation and raises
461 surface temperature by 2-4 °C over high latitude regions compared to the control run (Fig. 7 top-
462 right and bottom-right panels). In experiments where bias correction was not applied
463 (2.5k_PI_x_x, 2.5k_PI_x_GISS and 2.5k_GS_x_GISS), the relatively cold conditions simulated
464 by the coupled model system shows an opposite albedo-vegetation response (> 3 °C cooling over
465 Northern Hemisphere high latitudes). This strong drift towards a colder climate in the absence of
466 bias correction resulted in the continuous formation of sea ice that ultimately reaches the
467 (shallow) seabed, effectively creating land ice and eliminating the ocean from the gridcell-In
468 coupled model system experiments without bias correction, we terminated the iterative processes
469 when this freezing of the ocean to the seabed occurred, because this condition caused the model
470 to crash (2.5k_PI_x_x, 2.5k_PI_x_GISS, and 2.5k_GS_x_GISS).

471

472 At lower latitudes, albedo tends to show decreases relative to the standard boundary conditions
473 in all experiments, particularly over the forested areas of the equatorial regions and temperate
474 latitudes of the Northern Hemisphere. Over the northern Africa and the Indian subcontinent
475 changes in both albedo and surface temperature are more mixed. Albedo change in central and
476 northern Africa driven by a reduction in the area occupied by shrubs and an increase in bare soil
477 fraction. This pattern of increased albedo is more prevalent in simulations that were initialized
478 with Green Sahara land cover boundary conditions.

479



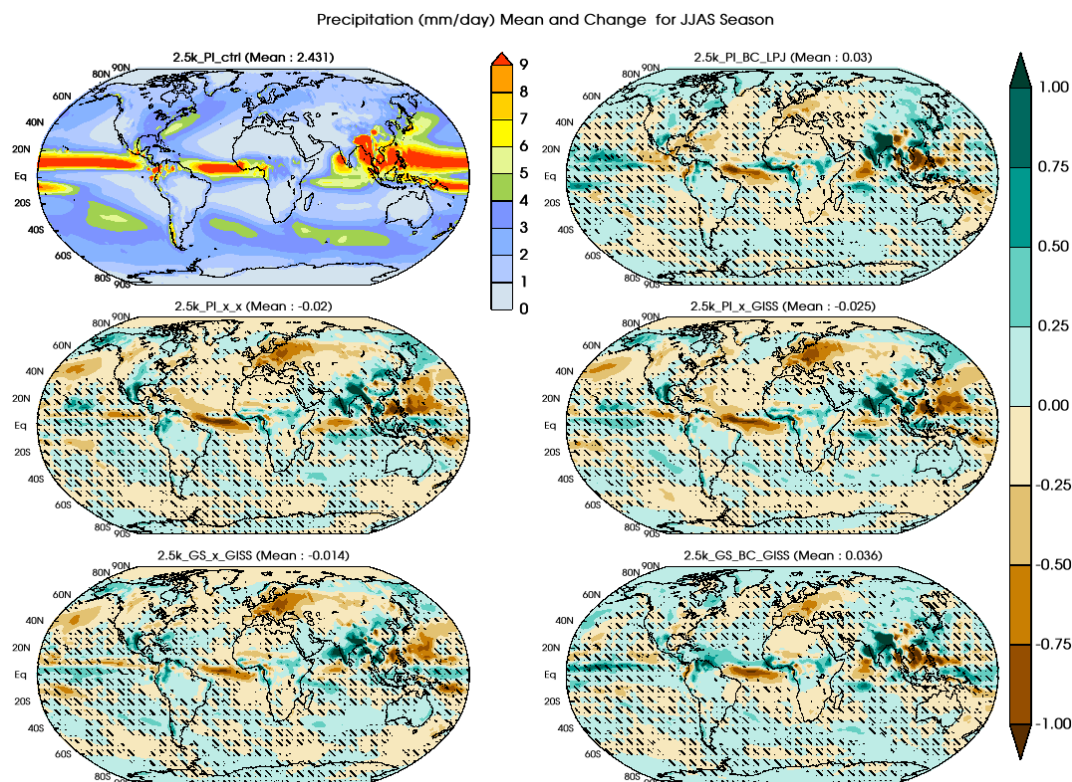
480
481 Figure 7. Same as figure 6 for Surface air temperature (°C) mean and change on an annual scale
482 (ANN season).

483
484 In experiments that were initialized with “Green Sahara” land cover boundary conditions where
485 interannual variability from GISS ModelE is included with and without adopting the bias
486 correction, comparison of the surface temperature response between simulations with
487 (2.5k_GS_x_GISS; Figure 7, bottom-left) and without bias correction (2.5k_GS_BC_GISS;
488 Figure 7, bottom-right) reveal the significance of bias correction for the asynchronous coupling
489 process. Broadly, we can observe that bias correction induces a warming of 0.7-0.8 °C, and
490 exclusion leads to a cooling of 0.9-1.1 °C, at the global scale, predominantly over the northern
491 hemisphere land regions.

492
493 Precipitation change across the model configurations is shown for Northern Hemisphere summer
494 (JJAS) at global scale in Figure 8. The significance of bias correction is noticeable over the high



495 latitudes of the Northern Hemisphere. Simulations with bias correction (2.5k_PI_BC_LPJ,
496 2.5k_GS_BC_GISS) lead to an increase in JJAS season precipitation relative to the initial
497 boundary conditions, while those experiments without bias correction (2.5k_PI_x_x,
498 2.5k_PI_x_GISS) show reductions in precipitation. Reductions in precipitation relative to initial
499 conditions are visible in Europe in all configurations and are greater in experiments where bias
500 correction was not applied. Another common feature among the experiments was the variable
501 spatial pattern of JJAS precipitation change over tropical regions. All configurations showed
502 increased precipitation over south and east Asia. Over the Nile headwaters in East Africa
503 (Melesse et al., 2011) precipitation increased, particularly in those experiments where bias
504 correction was applied. Interestingly, increased Northern Hemisphere summer monsoon
505 precipitation season (JJAS) over the Asian continent was simulated across all configurations. In
506 contrast, only a marginal northward procession of ITCZ over tropical Africa was simulated.
507



508
509



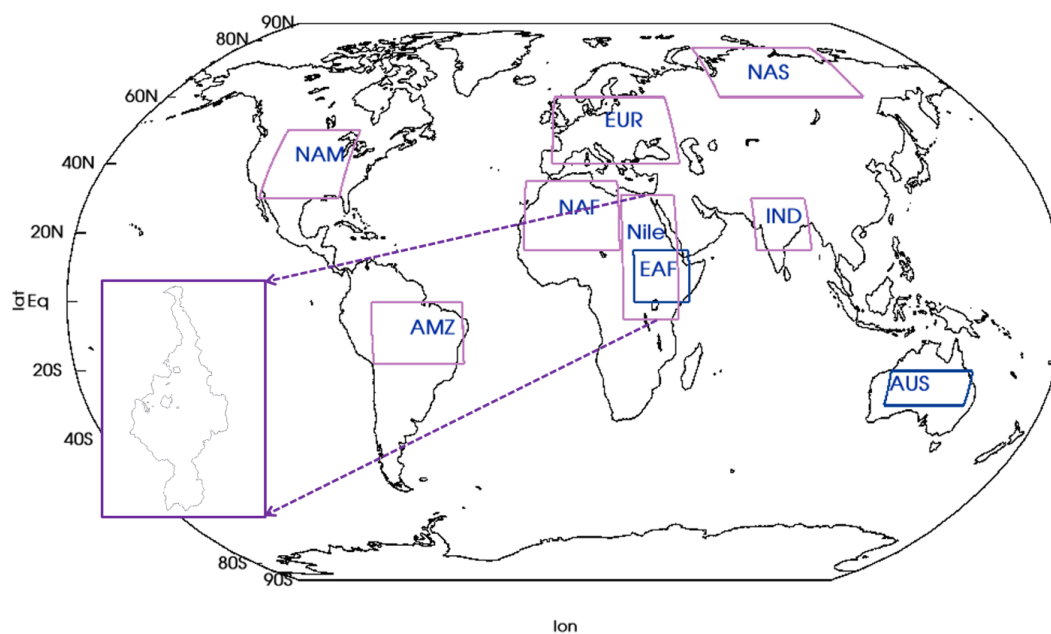
510 Figure 8. Same as figure 6 for precipitation (mm/day) mean and change on an annual scale (JJAS
511 season).

512

513 4.1 Regional climate

514 The spatial pattern of changes in climatic features for 2.5ka using our coupled model system
515 shows several prominent and robust regional signatures of climate change. We selected nine
516 regions over land (Fig. 9; Table 3) to analyze regional temperature and precipitation changes in
517 our simulations. Area-averaged time-series anomalies with respect to the 2.5ka control run
518 (2.5k_PI_ctrl) for the various experiments performed are calculated for these different regions.

519



520

521

522 Figure 9. Boundaries for the regions used for regional analysis. The inset map shows the Nile
523 River basin in high resolution, which is superimposed upon the ModelE resolution to generate
524 the grid-specific weights for the Nile River basin. The EAF and AUS regions are used in
525 Figs. 4A and 11.

526

527



528 **Table 3:** - Regions details including the boundary co-ordinates for all the regions.

Region (long name)	Region (short name)	Region boundary (Latitudes)	Region boundary (Longitudes)
North America	NAM	30°-50° N	115°-85° W
Amazon Rainforest Region	AMZ	0°-18° S	37°-70° W
Northern Asia (Siberia)	NAS	60°-77° N	70°-135° E
North Africa	NAF	15°-35° N	15° W-20° E
Europe	EUR	40°-60° N	5° W-45° E
Indian Region	IND	15°-30° N	70°-90° E
Nile River Basin	Nile	5° S-31° N	21°-41° E
East Africa	EAF	5°-15° N	25°-45° E
Australia	AUS	20°-30° S	120°-150° E

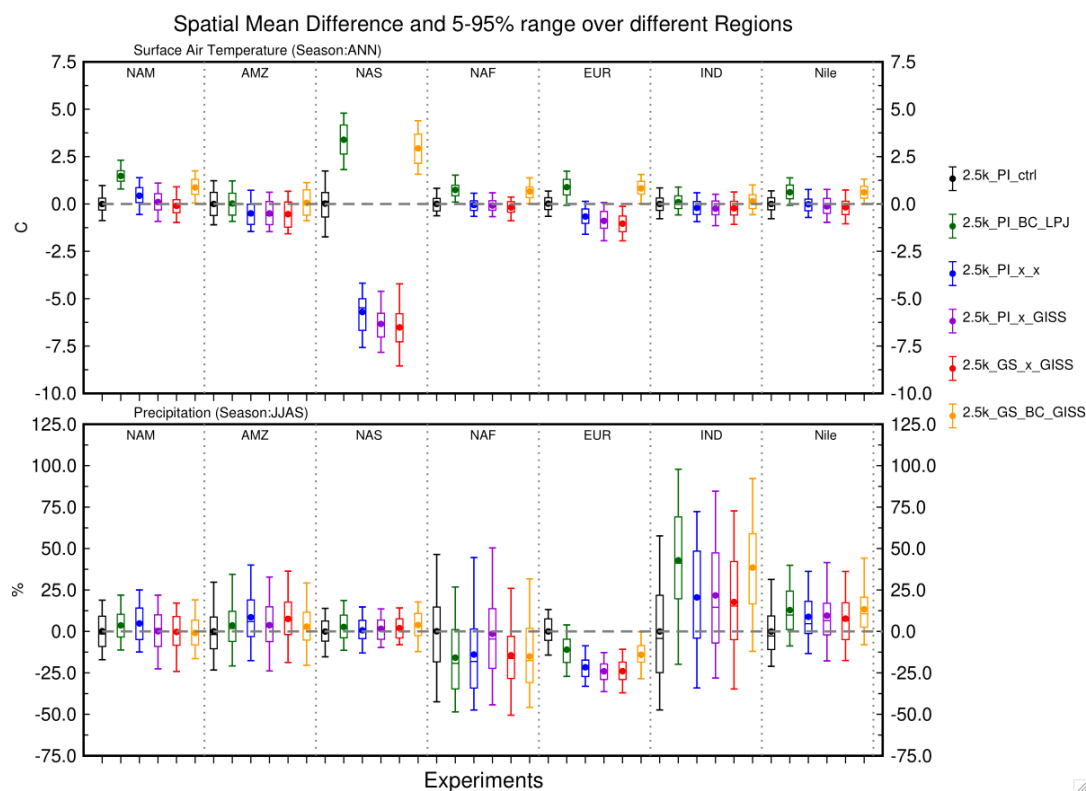
529

530 Figure 10 shows box-and-whisker plots of mean and median annual surface temperature (top)
 531 and JJAS seasonal precipitation (bottom) change, as well as the 5-95 percentile range along with
 532 the upper and lower quartiles (25th and 75th percentiles) of the anomaly time series for each
 533 region. As suggested from the global analyses of spatial patterns, the shift towards relatively
 534 warmer or colder climate as a result of applying bias correction is evident. Bias correction leads
 535 to strong warming over northern Asia (NAS region) of 3-4 °C, while without bias correction this
 536 region cools by 5-6 °C. The partition between experiments with and without bias correction is
 537 also apparent over selected regions of the mid-latitudes between 35°-60° N (NAS and EUP).

538

539 Except for northern Asia (NAS), all regions show approximately similar interannual variability
 540 in mean annual surface temperature. In northern Asia interannual variability is greater, especially
 541 in simulations where bias correction was not applied. Our results show that interannual
 542 variability in summer temperature in northern Asia is sensitive to changes in land cover, with
 543 greater variability in simulations where bias correction was not applied.

544



545
546 Figure 10. Regional change in surface air temperature (top panel, °C, annual mean) and
547 precipitation (bottom panel, %, JJAS) for the various simulations with respect to the 2.5ka control
548 run (2.5k_PI_ctrl). Regions name as listed in table 3.

549
550 Simulated 2.5ka precipitation for the Northern Hemisphere summer (JJAS) shows substantial
551 changes in mean state relative to the 2.5ka control with PI vegetations, particularly for the
552 tropical regions of northern Africa, India, and the Nile basin (Fig. 10, bottom panel). Interannual
553 variability in precipitation is comparable to the initial control run (black line). However, the
554 magnitude of variability differs across the regions; it is more prominent in tropical regions than
555 in the extratropics. An increase in mean precipitation of order of 20-30% without bias correction
556 and up to 40% with bias correction is simulated in JJAS season precipitation for the Indian
557 summer monsoon region (IND and it is in a range of 10-25% increase over the Nile basin region.
558 A drying pattern over Europe (EUR) ranges from 10-25% and is consistent for all the
559 simulations; a greater decrease in European precipitation was simulated when bias correction is

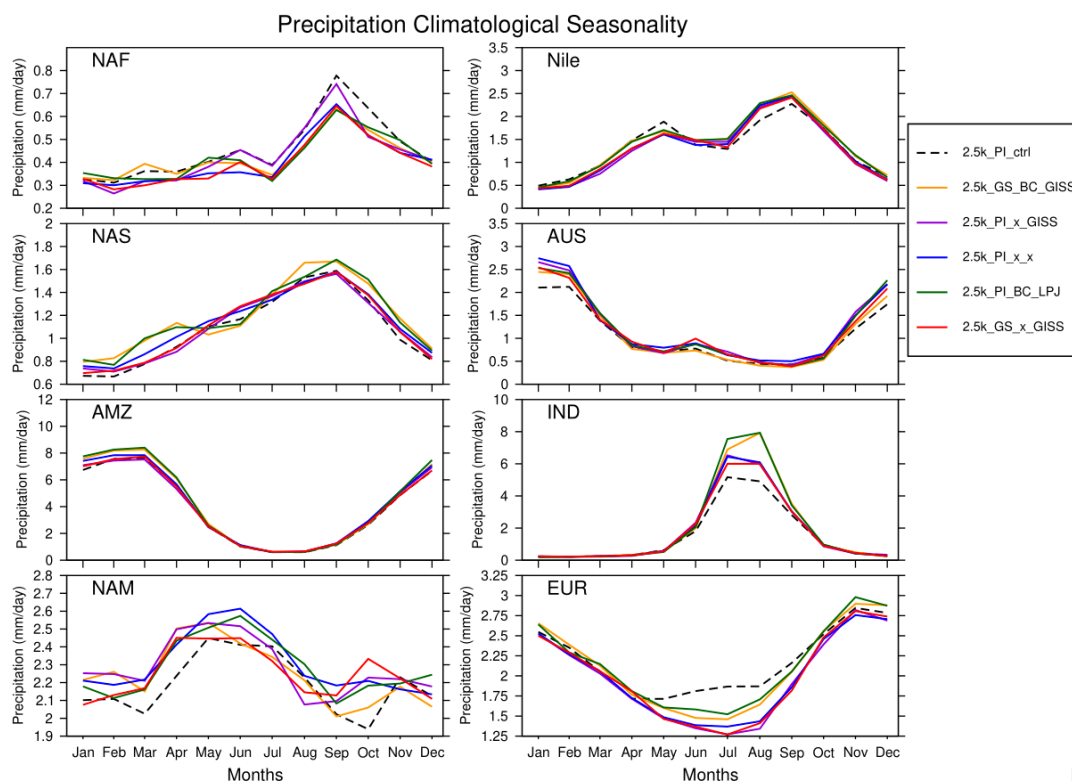


560 not adopted. A similar drying pattern was also simulated over the North America (NAM) and
561 northern Africa (NAF) regions. The relatively small magnitude of interannual variability in
562 precipitation over Europe and North America suggests that model does not produce high
563 variability across these regions and that it is not sensitive to the different experimental
564 configurations. Despite the large changes in both mean state and variability in temperature,
565 precipitation over northern Asia (NAS) changes little from the control state and across
566 simulations. In the Amazon region (AMZ), precipitation changes were small and not
567 significantly different between simulations. Without bias correction, the coupled model system
568 suggests a modest increase in mean seasonal precipitation up to 10%. We also noticed a similar
569 response of slightly increased precipitation in Southern Hemisphere summer (DJF) over
570 Australia (not shown here).

571

572 We further investigated the way our experiments influenced the seasonal cycle of temperature
573 and precipitation over the regions discussed above. Our results show that the seasonal cycle of
574 surface temperature is broadly similar across experiments for all the equatorial regions except the
575 Amazon (AMZ) region, where surface temperature is reduced by 0.5 °C in experiments where
576 bias correction was not applied (Fig. S3). Over the northern Asia (NAS) region, we see a
577 considerable difference in the seasonal cycle of temperature of 5-15 °C between runs with and
578 without bias correction. The seasonal cycle of temperature in the 2.5ka control (2.5k_PI_ctrl)
579 simulation over NAS is intermediate to the experiments but tracks closer to the simulations
580 where bias correction was applied, particularly in Northern Hemisphere winter, where, as noted
581 above, simulations without bias correction result in very cold conditions in this region.

582



583

584 Figure 11. Seasonality of precipitation averaged over the selected regions.

585

586 Compared to temperature, the seasonal cycle of precipitation shows greater differences among
587 simulations over several of the regions (Fig. 11). An increase of 2-3 mm/day over the Indian
588 region (IND) is simulated during the Indian Summer Monsoon months (JJAS) when using LPJ-
589 LMfire-generated land cover for both types of experiments (with and without bias correction),
590 with the bias-corrected simulations showing a larger increase in precipitation than the non-bias-
591 corrected ones. When bias correction is applied, the seasonal peak of precipitation shifts from
592 July to August. Over Europe, we observe a decrease of up to 0.5 mm/day in summer
593 precipitation relative to the control simulation in all simulations that use the LPJ-LMfire PFTs.
594 Precipitation decreases even more when the bias correction was not applied. The North Africa
595 region (NAF) also shows a slight decrease in precipitation relative to the control over most of the
596 seasonal cycle, while in North America (NAM) we see an increase in precipitation outside of the
597 JJAS summer months. The Amazon rainforest region (AMZ) shows no change in the seasonal
598 cycle of precipitation in all experiments. The Nile River basin (Nile) and Australian (AUS)



599 regions also show small increases in precipitation relative to the control in their respective
600 monsoon seasons (JJAS and DJF).

601

602 **5.0 Comparison with paleoclimate-proxy records for 2.5ka**

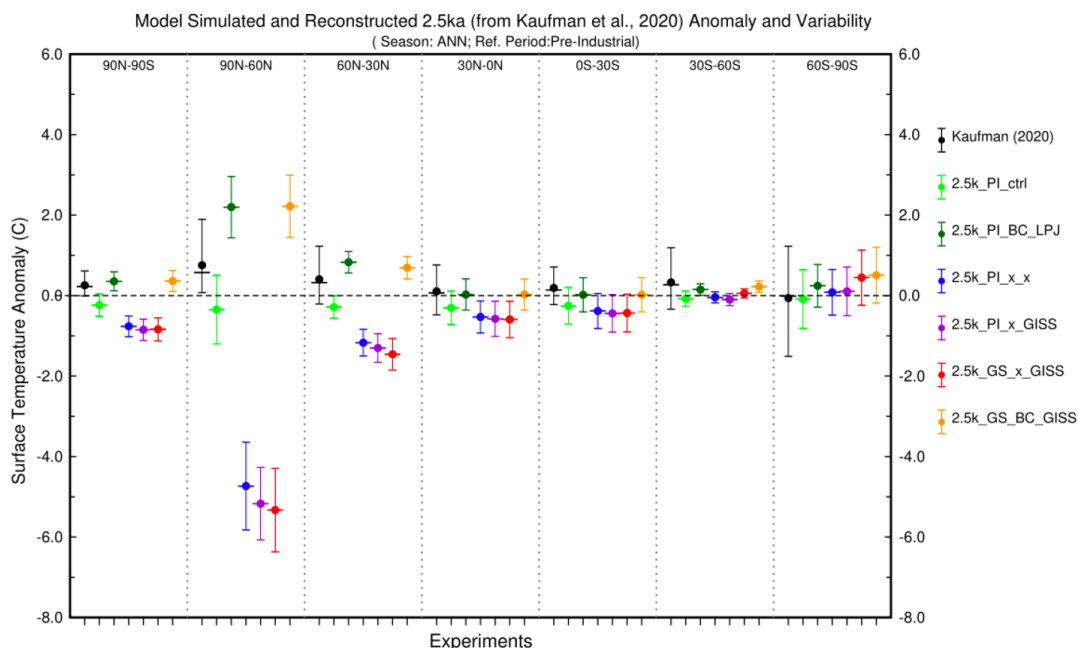
603 To evaluate the coupled model system's skill in representing past climate, we compared our
604 simulations for 2.5ka with multiproxy temperature reconstructions and speleothem-based oxygen
605 isotope records.

606

607 **5.1 Comparisons with reconstructed temperature**

608 Kaufman et al. (2020) used five different statistical methods to reconstruct temperature at 1319
609 globally distributed sites covering part or all of Holocene from a range of proxy types. For each
610 method, a 500-member ensemble of plausible reconstructions was presented. For comparison
611 with our model output, we extracted temperature anomalies for 2.5ka (relative to the value
612 reconstructed for the late preindustrial Holocene) from the ensemble reconstructions which we
613 binned into six latitude bands between the North and South Poles (each 30 degrees wide). We
614 computed the mean and median zonal anomaly using all 500 estimates of mean surface
615 temperature (MST) over each band for each of the five methodologies (total 2500), along with
616 the 5-95 percentile interval to represent uncertainty/variability among the sites in the zone and
617 across reconstruction methods (black bar in Figure 12) as suggested (Kaufman et al. 2020).

618



619

620 Figure 12: Comparison of model simulated annual surface temperature anomalies and interannual
621 variability for 2.5ka (with LPJ-LMfire vegetation) against the independent proxy-based
622 temperature reconstructions (black, Kaufman et al., 2020). Mean (circle), median (line) along with
623 5-95 percentile range as variability bars (whiskers) and different colors represent our different
624 experiments.

625

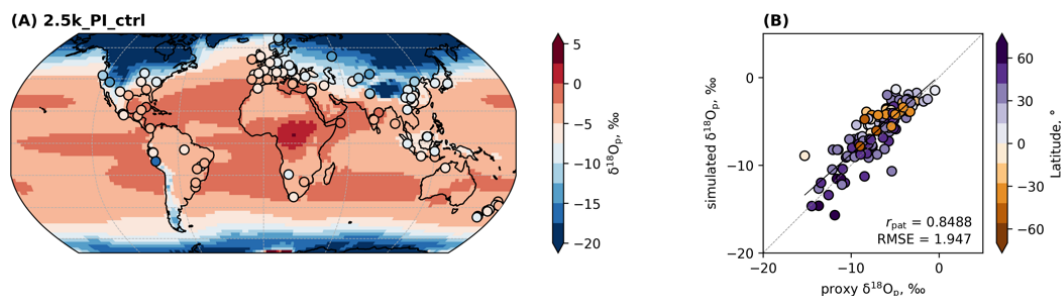
626 On global mean and in all latitude bands except the most southern one, proxy reconstructed
627 surface temperature is slightly warmer at 2.5ka relative to the late preindustrial. Model
628 simulations where bias correction was not applied show colder conditions than the
629 reconstructions globally and in the Northern Hemisphere. These differences between model and
630 proxy are very large in the high latitudes of the Northern Hemisphere and statistically significant
631 throughout the extra-tropics. In the Southern Hemisphere, the differences between model and
632 proxy reconstructions are smaller and insignificant, and there is less difference between
633 simulations with and without bias correction. It should be noted that the larger uncertainty in
634 reconstructed temperature over the southern polar band is due to a noticeably lower number of
635 available proxy records (157 records; Kaufman et al., 2020).

636



637 5.2 Comparisons with speleothem oxygen isotope ratios

638 ModelE2.1 includes a representation of the stable water isotopologues as passive tracers and the
639 isotopic composition of precipitation can be diagnosed from the model output. We compared the
640 simulated mean annual isotopic composition of precipitation ($\delta^{18}\text{O}_p$) with oxygen isotope records
641 from the Speleothem Isotope Synthesis and Analysis (SISAL) version 2 database (Comas-Bru et
642 al., 2020). Using the published chronologies for each speleothem record we extracted all samples
643 dated between 3-2 ka, which resulted in 163 measurements from 111 sites. Depending on their
644 mineralogy (i.e., calcite or aragonite), the mean $\delta^{18}\text{O}$ values (VPDB) were converted to their drip
645 water equivalents that could be compared to simulated $\delta^{18}\text{O}_p$ (VSMOW) (Comas-Bru et al.,
646 2020). We used simulated mean surface air temperature obtained from the grid points nearest
647 each cave sites to estimate the cave temperature required to convert mineral $\delta^{18}\text{O}$ to an
648 equivalent the drip water value. For each of our model experiments, we extracted simulated
649 $\delta^{18}\text{O}_p$ nearest to each cave site and compared it with the estimated drip-water $\delta^{18}\text{O}$.
650 Overall, the mean $\delta^{18}\text{O}_p$ spatial distribution in all 2.5ka simulations is in excellent agreement
651 with the proxies, showing better pattern correlations (r_{pat}) than 0.83 (Figure 13), with
652 the 2.5k_PI_x_x iteration marginally showing the highest skill (i.e., $r_{pat} = 0.85$ and RMSE =
653 1.90; shown in supplementary Fig S4). For comparison, the worst simulation using this metric,
654 2.5k_GS_BC_GISS, is almost as equally skillful ($r_{pat} = 0.84$ and RMSE = 1.92; Fig. S4),
655 demonstrating that none of the different configurations we presented here were significantly
656 different.



657
658 Figure 13. Comparison of simulated $\delta^{18}\text{O}_p$ with speleothem $\delta^{18}\text{O}$. Left: global distribution (70° S-
659 70° N) of simulated $\delta^{18}\text{O}_p$ (background) and speleothem $\delta^{18}\text{O}$ (circles), converted to their drip
660 water equivalents (see text) for the 2.5k_PI_ctrl simulation. Right: scatterplots between simulated
661 and proxy $\delta^{18}\text{O}_p$. Black line represents the least squares regression fits to data points while the gray



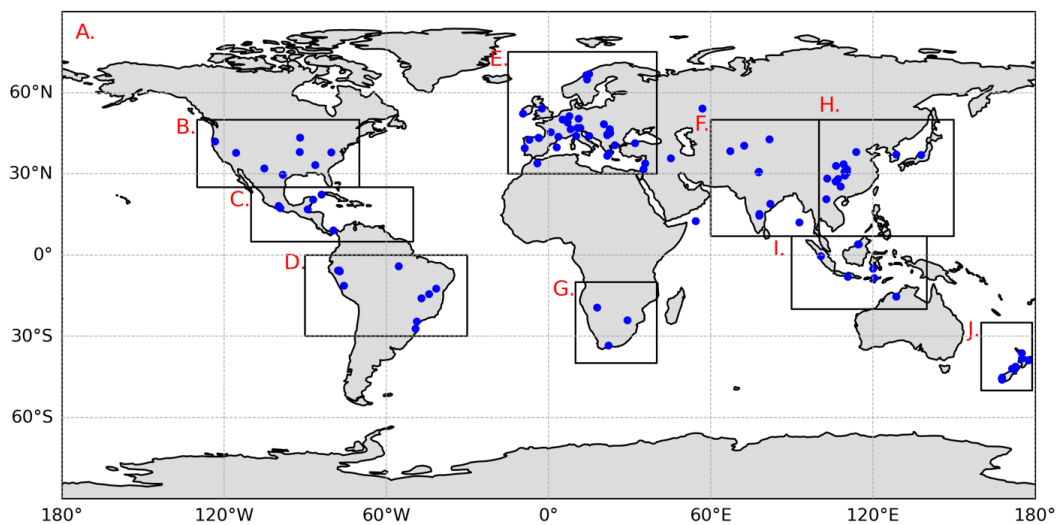
662 dashed line represents the 1:1 line. r_{pat} and RMSE are reported in the lower right corner of the
663 scatterplot. For comparison against each model experiment, see Fig. S4

664

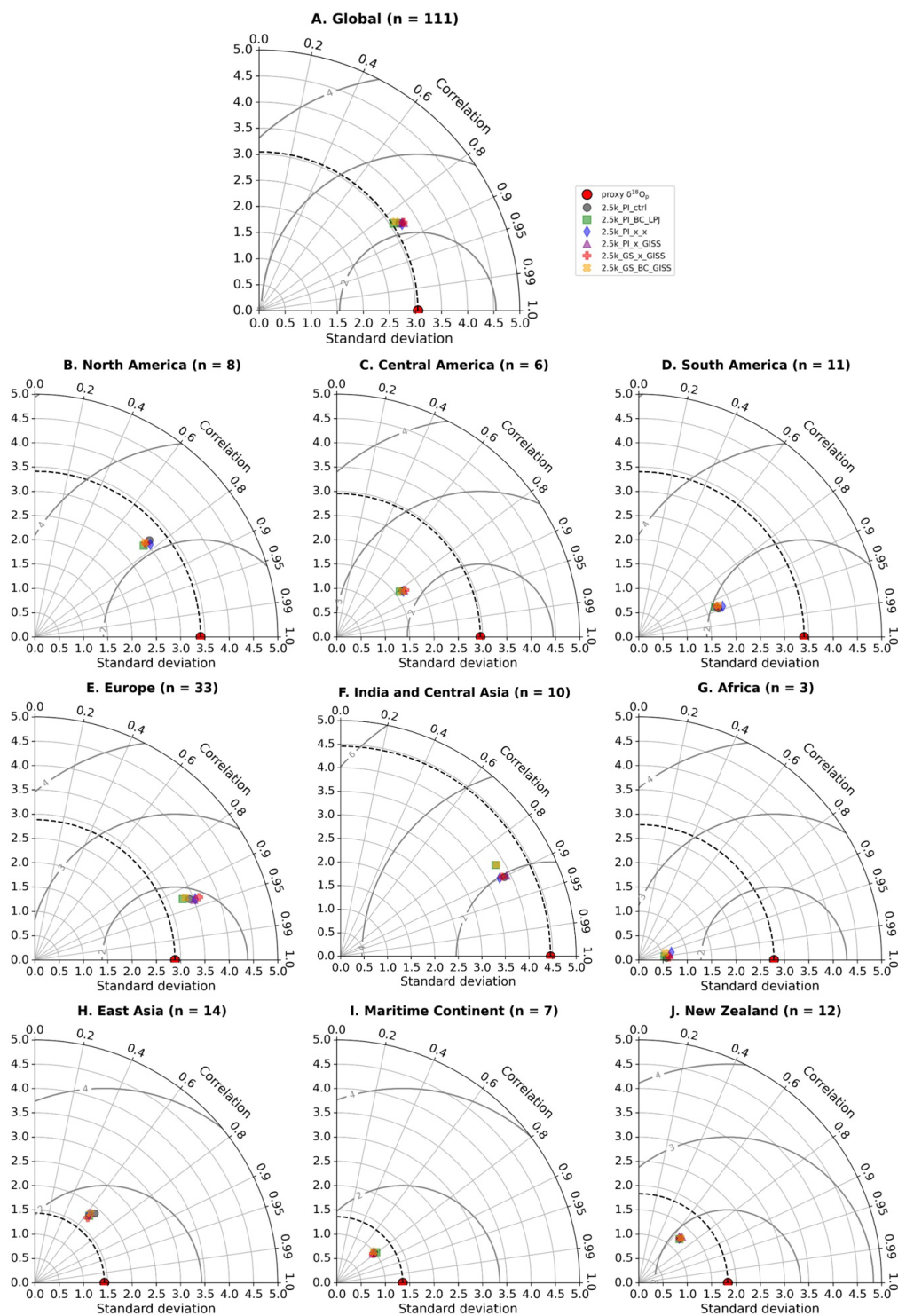
665 Regionally, we similarly found that most simulations show no significant deviation with each
666 other (Figure 14, Figure 15). We note, however, that over Europe (Figure 15E), variability may
667 be explained by the observed change in magnitude on both SAT and summer precipitation
668 among simulations (Figure 7, 8, 10). Over India and Central Asia (Figure 15F), simulations with
669 bias correction show lower correlation and higher RMSE values compared to other models
670 against proxy $\delta^{18}O_p$. This is likely related to the observed increase in mean summer precipitation
671 over this region (Figure 10) that were not reflected in the proxy sites.

672

673 Compared to proxy $\delta^{18}O_p$, simulations over certain regions show better agreement. Europe,
674 which is the most densely sampled region, show the best agreement with the proxies (i.e., high
675 correlation, closest to the reference point, Figure 15E) with the 2.5k_PI_x_GISS iteration best
676 capturing the spatial $\delta^{18}O_p$ pattern (i.e., $r_{pat} = 0.94$ and RMSE = 1.26). In contrast, simulations
677 over Central America, South America and Africa show the least skill where the magnitude of
678 $\delta^{18}O_p$ change are consistently underestimated (i.e., moderate to high correlation but farthest away
679 from the reference point). This may largely be due to inadequate sampling in these regions,
680 especially for Africa, and/or both precipitation and SAT influencing $\delta^{18}O$ may be underestimated
681 at these proxy locations, resulting in a generally muted $\delta^{18}O$ response across simulations. Cave-
682 specific factors that alter speleothem $\delta^{18}O$ (e.g., groundwater mixing, fractionation, (Baker et al.,
683 2019; Hartmann and Baker, 2017; Lachniet, 2009) are also not effectively reproduced in the
684 models, contributing to the proxy-model mismatch. Regions where the largest simulated SAT,
685 precipitation, and $\delta^{18}O_p$ change relative to the 2.5k_PI_ctrl are observed, such as northern Africa,
686 the Amazon basin and Siberia, are not adequately represented by reconstructions, highlighting
687 the need to expand the proxy network to marine-based records and polar regions over the period
688 of interest to capture the full range of isotopic variation.



689
690 Figure 14. Demarcation of each geographical region. Labels A to J correspond to the respective
691 Taylor diagram plots in Figure 15.





693 Figure 15. Taylor diagrams showing the r , SD and RMSE values between the proxy-derived and
694 simulated $\delta^{18}\text{O}_p$ for each 2.5k iteration globally (A) and at each subregion (B to J). Subregions are
695 demarcated in supporting figure 14.

696 **6.0 Discussion and Conclusions**

697 Here we presented a generalized technical framework for asynchronously coupling a climate
698 model (NASA GISS ModelE2.1) with a dynamic vegetation model (LPJ-LMfire) i.e., the “coupled
699 model system”, and demonstrate its skill in reconstructing climate in the late preindustrial
700 Holocene and for 2.5ka. We examined the role of bias and interannual variability corrections in
701 this process, and showed how they influence simulated land cover and climate. We demonstrated
702 the importance of considering such metrics in such a framework in our experimental design and
703 global and regional scale analyses. We performed a detailed evaluation and comparison of the
704 climate simulated by the coupled model system with reconstructions of air temperature (Kaufman
705 et al., 2020) and the isotopic composition of precipitation ($\delta^{18}\text{O}_p$) based on speleothems (Comas-
706 Bru et al., 2020). Similarly to previous studies that used asynchronous coupling to simulate
707 regional and global paleoclimate (Kjellstrom et al., 2008; Texier et al., 1997; Noblet et al., 1997;
708 Velasquez et al., 2021; Claussen, 2009; Strandberg et al., 2011, 2014), we assessed the influence
709 of the biogeophysical feedback between land and atmosphere.

710 Our results demonstrate the strong influence of including bias correction when passing simulated
711 climate to the land surface model. To correct biases inherent in the climate model, in selected
712 experiments we passed climate anomalies relative to a control simulation to the land model that
713 were added to a standard baseline climatology based on contemporary observations. In simulations
714 without this bias correction, raw simulated climate was passed directly from ModelE to LPJ-
715 LMfire. Where bias correction was applied ModelE drifts towards warmer climate; simulations
716 without bias correction drift towards colder climate. This effect was especially apparent in the high
717 latitudes of the Northern Hemisphere, particularly over Asia. With bias correction, high latitude
718 vegetation is dominated by tree plant functional types, while without it, cold shrubs and arctic
719 grasses are the predominant form of land cover. These results are characteristic of the well-known
720 vegetation-albedo feedback that is important at high latitudes (Charney et al., 1977; Charney,
721 1975; Doughty et al., 2012, 2018; Pang et al., 2022; Stocker et al., 2013; Swann et al., 2010; Zeng
722 et al., 2021).

723



724 The effects of bias correction on precipitation were less apparent and confined to regional scale.
725 We simulated a greater Indian summer monsoon season (JJAS) precipitation with bias correction
726 (>1 mm/day), and a nominal increase of ~ 0.5 mm/day across east China, Africa, and the North
727 American monsoon region. In other regions, the patterns of precipitation change were similar
728 across all experiments except for Europe where drier conditions are simulated in summer (up to $-$
729 1 mm/day) in simulations where bias correction was not applied.

730

731 The high latitudes of the Northern Hemisphere were also the region with the largest disagreement
732 between model and independent, multi-proxy temperature reconstructions. These comparisons
733 also highlighted the important role of bias correction; experiments with correction were much more
734 similar to reconstructions than those without. Simulations of the isotopic composition of
735 precipitation ($\delta^{18}\text{O}_p$) shows an excellent agreement with speleothem records with a pattern
736 correlation greater than 0.8. However, the difference in the magnitude of model simulated $\delta^{18}\text{O}_p$
737 from proxies over various regions indicates an underestimation of relationship between surface
738 temperature and $\delta^{18}\text{O}_p$ variability (Henderson et al., 2006; Kurita et al., 2004). A global evaluation
739 of model skill is hindered by the difference in the number of independent paleoclimate
740 reconstructions available for different regions, particularly in north Asia where we see the greatest
741 sensitivity of the coupled model system to the experimental setup. When examining modeled and
742 reconstructed $\delta^{18}\text{O}_p$, in Europe, which is the region with the greatest number of records, we see a
743 stronger pattern correlation with lower RMS values as compared to other regions.

744

745 In this study, we confirmed the importance of the land surface for simulating paleoclimate, even
746 for the late Holocene where land surface conditions were not as different from present as they were
747 during, e.g., the last glacial cycle or even mid-Holocene. We demonstrated that asynchronous
748 coupling can be a computationally inexpensive way of capturing land-atmosphere feedbacks and
749 improving the fidelity of the simulated climate. We noted that correcting bias present in the climate
750 model is essential for simulating climate that is consistent with independent reconstructions,
751 particularly for the high latitudes of the Northern Hemisphere. Future work with the coupled model
752 system will include quantification of the influence of major volcanic eruptions for regional and
753 global paleoclimate (Singh et al., 2024, in preparation) and the influence of past climate on the
754 dynamics of complex civilizations in prehistory.



755 **Code/Data availability**

756 Details to support the results in the manuscript is available as supplementary information is
757 provided with the manuscript. GISS Model code snapshots are available at
758 <https://simplex.giss.nasa.gov/snapshots/> (National Aeronautics and Space Administration, 2024),
759 LPJ-LMFire (<https://zenodo.org/records/5831747>), and important codes, calculated diagnostics as
760 well as other relevant details are available at zenodo repository
761 (<https://doi.org/10.5281/zenodo.13626434>) (Singh et al., 2024). However, raw model outputs data
762 and codes are available on request from author due to large data volume.

763

764 **Acknowledgements**

765 RS, KT, ANL and FL acknowledge support by the National Science Foundation under Grant No.
766 ICER-1824770. ANL acknowledges institutional support from NASA GISS. Resources
767 supporting this work were provided by the NASA High-End Computing (HEC) Program through
768 the NASA Center for Climate Simulation (NCCS) at Goddard Space Flight Center and from the
769 Department of Earth Sciences at The University of Hong Kong. The authors thank for their input
770 through multiple discussions the project members and collaborators of the ICER-1824770 project,
771 ‘Volcanism, Hydrology and Social Conflict: Lessons from Hellenistic and Roman-Era Egypt and
772 Mesopotamia’. RS and FL acknowledge additional support from European Research Council grant
773 agreement no. 951649 (4-OCEANS project).

774

775 **Author’s contributions**

776 RS, KT and ANL identified the study period in consultation with the other authors and RS, AK,
777 KT, ANL and JOK designed the asynchronous coupling framework. RS and AK implemented it
778 and performed the simulations using NASA GISS ModelE and LPJ-LMfire models. IA and RR
779 provided the essential technical support while implementing the framework. RS and RDR created
780 the figures in close collaboration with KT, ANL. RS wrote the first draft of the manuscript and
781 RDR, KT, ANL, and JOK led the writing of subsequent drafts. All authors contributed to the
782 interpretation of results and the drafting of the text.

783 **Competing interests**

784 The authors declare no competing interests.

785



786 **Short Summary**

787 This study presents and demonstrates an experimental framework for asynchronous land-
788 atmosphere coupling using the NASA GISS ModelE and LPJ-LMfire models for the 2.5ka period.
789 This framework addresses the limitation of NASA ModelE, which does not have a fully dynamic
790 vegetation model component. It also shows the role of model performance metrics, such as model
791 bias and variability, and the simulated climate is evaluated against the multi-proxy paleoclimate
792 reconstructions for the 2.5ka climate.

793

794 **References**

795 Baker, A., Hartmann, A., Duan, W., Hankin, S., Comas-Bru, L., Cuthbert, M. O., Treble, P. C.,
796 Banner, J., Genty, D., Baldini, L. M., Bartolomé, M., Moreno, A., Pérez-Mejías, C., and Werner,
797 M.: Global analysis reveals climatic controls on the oxygen isotope composition of cave drip
798 water, *Nat Commun*, 10, 2984, <https://doi.org/10.1038/s41467-019-11027-w>, 2019.

799 Bauer, S. E., Tsigaridis, K., Faluvegi, G., Kelley, M., Lo, K. K., Miller, R. L., Nazarenko, L.,
800 Schmidt, G. A., and Wu, J.: Historical (1850–2014) Aerosol Evolution and Role on Climate
801 Forcing Using the GISS ModelE2.1 Contribution to CMIP6, *Journal of Advances in Modeling
802 Earth Systems*, 12, e2019MS001978, <https://doi.org/10.1029/2019MS001978>, 2020.

803 Berger, A., Loutre, M. F., and Mélice, J. L.: Equatorial insolation: from precession harmonics to
804 eccentricity frequencies, *Climate of the Past*, 2, 131–136, <https://doi.org/10.5194/cp-2-131-2006>,
805 2006.

806 Betts, R. A.: Offset of the potential carbon sink from boreal forestation by decreases in surface
807 albedo, *Nature*, 408, 187–190, <https://doi.org/10.1038/35041545>, 2000.

808 Braconnot, P., Harrison, S. P., Kageyama, M., Bartlein, P. J., Masson-Delmotte, V., Abe-Ouchi,
809 A., Otto-Bliesner, B., and Zhao, Y.: Evaluation of climate models using palaeoclimatic data,
810 *Nature Clim Change*, 2, 417–424, <https://doi.org/10.1038/nclimate1456>, 2012.

811 Chandan, D. and Peltier, W. R.: African Humid Period Precipitation Sustained by Robust
812 Vegetation, Soil, and Lake Feedbacks, *Geophysical Research Letters*, 47, e2020GL088728,
813 <https://doi.org/10.1029/2020GL088728>, 2020.

814 Charney, J., Quirk, W. J., Chow, S., and Kornfield, J.: A Comparative Study of the Effects of
815 Albedo Change on Drought in Semi-Arid Regions, *Journal of the Atmospheric Sciences*, 34,
816 1366–1385, [https://doi.org/10.1175/1520-0469\(1977\)034<1366:ACSOTE>2.0.CO;2](https://doi.org/10.1175/1520-0469(1977)034<1366:ACSOTE>2.0.CO;2), 1977.

817 Charney, J. G.: Dynamics of deserts and drought in the Sahel, *Quarterly Journal of the Royal
818 Meteorological Society*, 101, 193–202, <https://doi.org/10.1002/qj.49710142802>, 1975.

819 Claussen, M.: Modeling bio-geophysical feedback in the African and Indian monsoon region,
820 *Climate Dynamics*, 13, 247–257, <https://doi.org/10.1007/s003820050164>, 1997.



- 821 Collins, J. A., Prange, M., Caley, T., Gimeno, L., Beckmann, B., Mulitza, S., Skonieczny, C.,
822 Roche, D., and Schefuß, E.: Rapid termination of the African Humid Period triggered by
823 northern high-latitude cooling, *Nat Commun*, 8, 1372, [https://doi.org/10.1038/s41467-017-](https://doi.org/10.1038/s41467-017-01454-y)
824 01454-y, 2017.
- 825 Comas-Bru, L., Atsawawaranunt, K., Harrison, S., and members, S. working group: SISAL
826 (Speleothem Isotopes Synthesis and AnaLysis Working Group) database version 2.0,
827 <https://doi.org/10.17864/1947.256>, 2020.
- 828 Cox, P. M., Betts, R. A., Jones, C. D., Spall, S. A., and Totterdell, I. J.: Acceleration of global
829 warming due to carbon-cycle feedbacks in a coupled climate model, *Nature*, 408, 184–187,
830 <https://doi.org/10.1038/35041539>, 2000.
- 831 Dallmeyer, A., Claussen, M., Lorenz, S. J., Sigl, M., Toohey, M., and Herzschuh, U.: Holocene
832 vegetation transitions and their climatic drivers in MPI-ESM1.2, *Climate of the Past*, 17, 2481–
833 2513, <https://doi.org/10.5194/cp-17-2481-2021>, 2021.
- 834 Doherty, R., Kutzbach, J., Foley, J., and Pollard, D.: Fully coupled climate/dynamical vegetation
835 model simulations over Northern Africa during the mid-Holocene, *Climate Dynamics*, 16, 561–
836 573, <https://doi.org/10.1007/s003820000065>, 2000.
- 837 Doughty, C. E., Loarie, S. R., and Field, C. B.: Theoretical Impact of Changing Albedo on
838 Precipitation at the Southernmost Boundary of the ITCZ in South America, *Earth Interactions*,
839 16, 1–14, <https://doi.org/10.1175/2012EI422.1>, 2012.
- 840 Doughty, C. E., Santos-Andrade, P. E., Shenkin, A., Goldsmith, G. R., Bentley, L. P., Blonder,
841 B., Díaz, S., Salinas, N., Enquist, B. J., Martin, R. E., Asner, G. P., and Malhi, Y.: Tropical forest
842 leaves may darken in response to climate change, *Nat Ecol Evol*, 2, 1918–1924,
843 <https://doi.org/10.1038/s41559-018-0716-y>, 2018.
- 844 Eyring, V., Bony, S., Meehl, G. A., Senior, C. A., Stevens, B., Stouffer, R. J., and Taylor, K. E.:
845 Overview of the Coupled Model Intercomparison Project Phase 6 (CMIP6) experimental design
846 and organization, *Geoscientific Model Development*, 9, 1937–1958,
847 <https://doi.org/10.5194/gmd-9-1937-2016>, 2016.
- 848 Fekete, B. M., Vörösmarty, C. J., and Lammers, R. B.: Scaling gridded river networks for
849 macroscale hydrology: Development, analysis, and control of error, *Water Resources Research*,
850 37, 1955–1967, <https://doi.org/10.1029/2001WR900024>, 2001.
- 851 Gao, F., Morisette, J. T., Wolfe, R. E., Ederer, G., Pedelty, J., Masuoka, E., Myneni, R., Tan, B.,
852 and Nightingale, J.: An Algorithm to Produce Temporally and Spatially Continuous MODIS-
853 LAI Time Series, *IEEE Geoscience and Remote Sensing Letters*, 5, 60–64,
854 <https://doi.org/10.1109/LGRS.2007.907971>, 2008.
- 855 Hamilton, D. S., Hantson, S., Scott, C. E., Kaplan, J. O., Pringle, K. J., Nieradzik, L. P., Rap, A.,
856 Folberth, G. A., Spracklen, D. V., and Carslaw, K. S.: Reassessment of pre-industrial fire
857 emissions strongly affects anthropogenic aerosol forcing, *Nat Commun*, 9, 3182,
858 <https://doi.org/10.1038/s41467-018-05592-9>, 2018.



- 859 Harris, I., Osborn, T. J., Jones, P., and Lister, D.: Version 4 of the CRU TS monthly high-
860 resolution gridded multivariate climate dataset, *Sci Data*, 7, 109, [https://doi.org/10.1038/s41597-](https://doi.org/10.1038/s41597-020-0453-3)
861 020-0453-3, 2020.
- 862 Harrison, S. P., Bartlein, P. J., Izumi, K., Li, G., Annan, J., Hargreaves, J., Braconnot, P., and
863 Kageyama, M.: Evaluation of CMIP5 palaeo-simulations to improve climate projections, *Nature*
864 *Clim Change*, 5, 735–743, <https://doi.org/10.1038/nclimate2649>, 2015.
- 865 Hartmann, A. and Baker, A.: Modelling karst vadose zone hydrology and its relevance for
866 paleoclimate reconstruction, *Earth-Science Reviews*, 172, 178–192,
867 <https://doi.org/10.1016/j.earscirev.2017.08.001>, 2017.
- 868 Henderson, K., Laube, A., Gäggeler, H. W., Olivier, S., Papina, T., and Schwikowski, M.:
869 Temporal variations of accumulation and temperature during the past two centuries from
870 Belukha ice core, Siberian Altai, *Journal of Geophysical Research: Atmospheres*, 111,
871 <https://doi.org/10.1029/2005JD005819>, 2006.
- 872 Hoesly, R. M., Smith, S. J., Feng, L., Klimont, Z., Janssens-Maenhout, G., Pitkanen, T., Seibert,
873 J. J., Vu, L., Andres, R. J., Bolt, R. M., Bond, T. C., Dawidowski, L., Kholod, N., Kurokawa, J.,
874 Li, M., Liu, L., Lu, Z., Moura, M. C. P., O'Rourke, P. R., and Zhang, Q.: Historical (1750–2014)
875 anthropogenic emissions of reactive gases and aerosols from the Community Emissions Data
876 System (CEDS), *Geoscientific Model Development*, 11, 369–408, [https://doi.org/10.5194/gmd-](https://doi.org/10.5194/gmd-11-369-2018)
877 11-369-2018, 2018.
- 878 Jahn, B., Schneider, R. R., Müller, P.-J., Donner, B., and Röhl, U.: Response of tropical African
879 and East Atlantic climates to orbital forcing over the last 1.7 Ma, *Geological Society, London,*
880 *Special Publications*, 247, 65–84, <https://doi.org/10.1144/GSL.SP.2005.247.01.04>, 2005.
- 881 Kageyama, M., Braconnot, P., Harrison, S. P., Haywood, A. M., JungCLAUS, J. H., Otto-Bliesner,
882 B. L., Peterschmitt, J.-Y., Abe-Ouchi, A., Albani, S., Bartlein, P. J., Brierley, C., Crucifix, M.,
883 Dolan, A., Fernandez-Donado, L., Fischer, H., Hopcroft, P. O., Ivanovic, R. F., Lambert, F.,
884 Lunt, D. J., Mahowald, N. M., Peltier, W. R., Phipps, S. J., Roche, D. M., Schmidt, G. A.,
885 Tarasov, L., Valdes, P. J., Zhang, Q., and Zhou, T.: The PMIP4 contribution to CMIP6 – Part 1:
886 Overview and over-arching analysis plan, *Geoscientific Model Development*, 11, 1033–1057,
887 <https://doi.org/10.5194/gmd-11-1033-2018>, 2018.
- 888 Kaplan, J. O., Koch, A., and Vitali, R.: ARVE-Research/LPJ-LMfire: LPJ-LMfire (tropical
889 forest restoration), , <https://doi.org/10.5281/zenodo.5831747>, 2022.
- 890 Kattge, J., Díaz, S., Lavorel, S., Prentice, I. C., Leadley, P., Bönisch, G., Garnier, E., Westoby,
891 M., Reich, P. B., Wright, I. J., Cornelissen, J. H. C., Violle, C., Harrison, S. P., Van BODEGOM,
892 P. M., Reichstein, M., Enquist, B. J., Soudzilovskaia, N. A., Ackerly, D. D., Anand, M., Atkin,
893 O., Bahn, M., Baker, T. R., Baldocchi, D., Bekker, R., Blanco, C. C., Blonder, B., Bond, W. J.,
894 Bradstock, R., Bunker, D. E., Casanoves, F., Cavender-Bares, J., Chambers, J. Q., Chapin Iii, F.
895 S., Chave, J., Coomes, D., Cornwell, W. K., Craine, J. M., Dobrin, B. H., Duarte, L., Durka, W.,
896 Elser, J., Esser, G., Estiarte, M., Fagan, W. F., Fang, J., Fernández-Méndez, F., Fidelis, A.,
897 Finegan, B., Flores, O., Ford, H., Frank, D., Freschet, G. T., Fyllas, N. M., Gallagher, R. V.,
898 Green, W. A., Gutierrez, A. G., Hickler, T., Higgins, S. I., Hodgson, J. G., Jalili, A., Jansen, S.,



- 899 Joly, C. A., Kerkhoff, A. J., Kirkup, D., Kitajima, K., Kleyer, M., Klotz, S., Knops, J. M. H.,
900 Kramer, K., Kühn, I., Kurokawa, H., Laughlin, D., Lee, T. D., Leishman, M., Lens, F., Lenz, T.,
901 Lewis, S. L., Lloyd, J., Llusà, J., Louault, F., Ma, S., Mahecha, M. D., Manning, P., Massad, T.,
902 Medlyn, B. E., Messier, J., Moles, A. T., Müller, S. C., Nadrowski, K., Naeem, S., Niinemets,
903 Ü., Nöllert, S., Nüske, A., Ogaya, R., Oleksyn, J., Onipchenko, V. G., Onoda, Y., Ordoñez, J.,
904 Overbeck, G., et al.: TRY – a global database of plant traits, *Global Change Biology*, 17, 2905–
905 2935, <https://doi.org/10.1111/j.1365-2486.2011.02451.x>, 2011.
- 906 Kaufman, D., McKay, N., Routson, C., Erb, M., Dätwyler, C., Sommer, P. S., Heiri, O., and
907 Davis, B.: Holocene global mean surface temperature, a multi-method reconstruction approach,
908 *Sci Data*, 7, 201, <https://doi.org/10.1038/s41597-020-0530-7>, 2020.
- 909 Kelley, M., Schmidt, G. A., Nazarenko, L. S., Bauer, S. E., Ruedy, R., Russell, G. L., Ackerman,
910 A. S., Aleinov, I., Bauer, M., Bleck, R., Canuto, V., Cesana, G., Cheng, Y., Clune, T. L., Cook,
911 B. I., Cruz, C. A., Del Genio, A. D., Elsaesser, G. S., Faluvegi, G., Kiang, N. Y., Kim, D., Lacis,
912 A. A., Leboissetier, A., LeGrande, A. N., Lo, K. K., Marshall, J., Matthews, E. E., McDermid,
913 S., Mezuman, K., Miller, R. L., Murray, L. T., Oinas, V., Orbe, C., García-Pando, C. P.,
914 Perlwitz, J. P., Puma, M. J., Rind, D., Romanou, A., Shindell, D. T., Sun, S., Tausnev, N.,
915 Tsigaridis, K., Tselioudis, G., Weng, E., Wu, J., and Yao, M.-S.: GISS-E2.1: Configurations and
916 Climatology, *Journal of Advances in Modeling Earth Systems*, 12, e2019MS002025,
917 <https://doi.org/10.1029/2019MS002025>, 2020.
- 918 Kim, Y., Moorcroft, P. R., Aleinov, I., Puma, M. J., and Kiang, N. Y.: Variability of phenology
919 and fluxes of water and carbon with observed and simulated soil moisture in the Ent Terrestrial
920 Biosphere Model (Ent TBM version 1.0.1.0.0), *Geoscientific Model Development*, 8, 3837–
921 3865, <https://doi.org/10.5194/gmd-8-3837-2015>, 2015.
- 922 Kubatzki, C. and Claussen, M.: Simulation of the global bio-geophysical interactions during the
923 Last Glacial Maximum, *Climate Dynamics*, 14, 461–471,
924 <https://doi.org/10.1007/s003820050234>, 1998.
- 925 Kurita, N., Yoshida, N., Inoue, G., and Chayanova, E. A.: Modern isotope climatology of Russia:
926 A first assessment, *Journal of Geophysical Research: Atmospheres*, 109,
927 <https://doi.org/10.1029/2003JD003404>, 2004.
- 928 Lachniet, M. S.: Climatic and environmental controls on speleothem oxygen-isotope values,
929 *Quaternary Science Reviews*, 28, 412–432, <https://doi.org/10.1016/j.quascirev.2008.10.021>,
930 2009.
- 931 Lamb, P. J.: Persistence of Subsaharan drought, *Nature*, 299, 46–48,
932 <https://doi.org/10.1038/299046a0>, 1982.
- 933 Louergue, L., Schilt, A., Spahni, R., Masson-Delmotte, V., Blunier, T., Lemieux, B., Barnola,
934 J.-M., Raynaud, D., Stocker, T. F., and Chappellaz, J.: Orbital and millennial-scale features of
935 atmospheric CH₄ over the past 800,000 years, *Nature*, 453, 383–386,
936 <https://doi.org/10.1038/nature06950>, 2008.



- 937 Ludlow, F. and Manning, J. G.: Volcanic Eruptions, Veiled Suns, and Nile Failure in Egyptian
938 History: Integrating Hydroclimate into Understandings of Historical Change, in: *Climate Change
939 and Ancient Societies in Europe and the Near East: Diversity in Collapse and Resilience*, edited
940 by: Erdkamp, P., Manning, J. G., and Verboven, K., Springer International Publishing, Cham,
941 301–320, https://doi.org/10.1007/978-3-030-81103-7_10, 2021.
- 942 Magi, B. I.: Global Lightning Parameterization from CMIP5 Climate Model Output, *Journal of
943 Atmospheric and Oceanic Technology*, 32, 434–452, [https://doi.org/10.1175/JTECH-D-13-
00261.1](https://doi.org/10.1175/JTECH-D-13-
944 00261.1), 2015.
- 945 Manning, J. G., Ludlow, F., Stine, A. R., Boos, W. R., Sigl, M., and Marlon, J. R.: Volcanic
946 suppression of Nile summer flooding triggers revolt and constrains interstate conflict in ancient
947 Egypt, *Nat Commun*, 8, 900, <https://doi.org/10.1038/s41467-017-00957-y>, 2017.
- 948 Mikhail, A.: Ottoman Iceland: A Climate History, *Environmental History*, 20, 262–284,
949 <https://doi.org/10.1093/envhis/emv006>, 2015.
- 950 Myneni, R. B., Hoffman, S., Knyazikhin, Y., Privette, J. L., Glassy, J., Tian, Y., Wang, Y., Song,
951 X., Zhang, Y., Smith, G. R., Lotsch, A., Friedl, M., Morisette, J. T., Votava, P., Nemani, R. R.,
952 and Running, S. W.: Global products of vegetation leaf area and fraction absorbed PAR from
953 year one of MODIS data, *Remote Sensing of Environment*, 83, 214–231,
954 [https://doi.org/10.1016/S0034-4257\(02\)00074-3](https://doi.org/10.1016/S0034-4257(02)00074-3), 2002.
- 955 Otto-Bliesner, B. L., Braconnot, P., Harrison, S. P., Lunt, D. J., Abe-Ouchi, A., Albani, S.,
956 Bartlein, P. J., Capron, E., Carlson, A. E., Dutton, A., Fischer, H., Goelzer, H., Govin, A.,
957 Haywood, A., Joos, F., LeGrande, A. N., Lipscomb, W. H., Lohmann, G., Mahowald, N.,
958 Nehrbass-Ahles, C., Pausata, F. S. R., Peterschmitt, J.-Y., Phipps, S. J., Renssen, H., and Zhang,
959 Q.: The PMIP4 contribution to CMIP6 – Part 2: Two interglacials, scientific objective and
960 experimental design for Holocene and Last Interglacial simulations, *Geoscientific Model
961 Development*, 10, 3979–4003, <https://doi.org/10.5194/gmd-10-3979-2017>, 2017.
- 962 Pang, G., Chen, D., Wang, X., and Lai, H.-W.: Spatiotemporal variations of land surface albedo
963 and associated influencing factors on the Tibetan Plateau, *Science of The Total Environment*,
964 804, 150100, <https://doi.org/10.1016/j.scitotenv.2021.150100>, 2022.
- 965 Pausata, F. S. R., Messori, G., and Zhang, Q.: Impacts of dust reduction on the northward
966 expansion of the African monsoon during the Green Sahara period, *Earth and Planetary Science
967 Letters*, 434, 298–307, <https://doi.org/10.1016/j.epsl.2015.11.049>, 2016.
- 968 Petit-Maire, N. and Guo, Z. T.: Mid-Holocene climatic change and man in the present-day
969 Sahara desert, in: *Quaternary Deserts and Climatic Change*, CRC Press, 1998.
- 970 Pfeiffer, M., Spessa, A., and Kaplan, J. O.: A model for global biomass burning in preindustrial
971 time: LPJ-LMfire (v1.0), *Geoscientific Model Development*, 6, 643–685,
972 <https://doi.org/10.5194/gmd-6-643-2013>, 2013.



- 973 Rachmayani, R., Prange, M., and Schulz, M.: North African vegetation–precipitation feedback in
974 early and mid-Holocene climate simulations with CCSM3-DGVM, *Climate of the Past*, 11, 175–
975 185, <https://doi.org/10.5194/cp-11-175-2015>, 2015.
- 976 Reale, O. and Dirmeyer, P.: Modeling the effects of vegetation on Mediterranean climate during
977 the Roman Classical Period: Part I: Climate history and model sensitivity, *Global and Planetary
978 Change*, 25, 163–184, [https://doi.org/10.1016/S0921-8181\(00\)00002-3](https://doi.org/10.1016/S0921-8181(00)00002-3), 2000.
- 979 Schneider, R., Schmitt, J., Köhler, P., Joos, F., and Fischer, H.: A reconstruction of atmospheric
980 carbon dioxide and its stable carbon isotopic composition from the penultimate glacial maximum
981 to the last glacial inception, *Climate of the Past*, 9, 2507–2523, [https://doi.org/10.5194/cp-9-
982 2507-2013](https://doi.org/10.5194/cp-9-
982 2507-2013), 2013.
- 983 Sha, L., Ait Brahim, Y., Wassenburg, J. A., Yin, J., Peros, M., Cruz, F. W., Cai, Y., Li, H., Du,
984 W., Zhang, H., Edwards, R. L., and Cheng, H.: How Far North Did the African Monsoon Fringe
985 Expand During the African Humid Period? Insights From Southwest Moroccan Speleothems,
986 *Geophysical Research Letters*, 46, 14093–14102, <https://doi.org/10.1029/2019GL084879>, 2019.
- 987 Shanahan, T. M., McKay, N. P., Hughen, K. A., Overpeck, J. T., Otto-Bliesner, B., Heil, C. W.,
988 King, J., Scholz, C. A., and Peck, J.: The time-transgressive termination of the African Humid
989 Period, *Nature Geosci*, 8, 140–144, <https://doi.org/10.1038/ngeo2329>, 2015.
- 990 Siegenthaler, U., Stocker, T. F., Monnin, E., Lüthi, D., Schwander, J., Stauffer, B., Raynaud, D.,
991 Barnola, J.-M., Fischer, H., Masson-Delmotte, V., and Jouzel, J.: Stable Carbon Cycle–Climate
992 Relationship During the Late Pleistocene, *Science*, 310, 1313–1317,
993 <https://doi.org/10.1126/science.1120130>, 2005.
- 994 Simard, M., Pinto, N., Fisher, J. B., and Baccini, A.: Mapping forest canopy height globally with
995 spaceborne lidar, *Journal of Geophysical Research: Biogeosciences*, 116,
996 <https://doi.org/10.1029/2011JG001708>, 2011.
- 997 Singh, R., Tsigaridis, K., LeGrande, A. N., Ludlow, F., and Manning, J. G.: Investigating
998 hydroclimatic impacts of the 168–158 BCE volcanic quartet and their relevance to the
999 Nile River basin and Egyptian history, *Climate of the Past*, 19, 249–275,
1000 <https://doi.org/10.5194/cp-19-249-2023>, 2023.
- 1001 Singh, R., Koch, A., LeGrande, A. N., Tsigaridis, K., Ramos, R. D., Ludlow, F., Aleinov, I.,
1002 Ruedy, R., and Kaplan, J. O.: Modelling framework for asynchronous land-atmosphere coupling
1003 using NASA GISS ModelE and LPJ-LMfire: Design, Application and Evaluation for the 2.5ka
1004 period, <https://doi.org/10.5281/zenodo.13626434>, 2024.
- 1005 Sitch, S., Smith, B., Prentice, I. C., Arneeth, A., Bondeau, A., Cramer, W., Kaplan, J. O., Levis,
1006 S., Lucht, W., Sykes, M. T., Thonicke, K., and Venevsky, S.: Evaluation of ecosystem dynamics,
1007 plant geography and terrestrial carbon cycling in the LPJ dynamic global vegetation model,
1008 *Global Change Biology*, 9, 161–185, <https://doi.org/10.1046/j.1365-2486.2003.00569.x>, 2003.
- 1009 Stocker, T. F., Qin, D., Plattner, G.-K., Tignor, M. M. B., Allen, S. K., Boschung, J., Nauels, A.,
1010 Xia, Y., Bex, V., Midgley, P. M., Alexander, L. V., Allen, S. K., Bindoff, N. L., Breon, F.-M.,



- 1011 Church, J. A., Cubasch, U., Emori, S., Forster, P., Friedlingstein, P., Gillett, N., Gregory, J. M.,
1012 Hartmann, D. L., Jansen, E., Kirtman, B., Knutti, R., Kumar Kanikicharla, K., Lemke, P.,
1013 Marotzke, J., Masson-Delmotte, V., Meehl, G. A., Mokhov, I. I., Piao, S., Plattner, G.-K., Dahe,
1014 Q., Ramaswamy, V., Randall, D., Rhein, M., Rojas, M., Sabine, C., Shindell, D., Stocker, T. F.,
1015 Talley, L. D., Vaughan, D. G., Xie, S.-P., Allen, M. R., Boucher, O., Chambers, D., Hesselbjerg
1016 Christensen, J., Ciais, P., Clark, P. U., Collins, M., Comiso, J. C., Vasconcellos de Menezes, V.,
1017 Feely, R. A., Fichfet, T., Fiore, A. M., Flato, G., Fuglestvedt, J., Hegerl, G., Hezel, P. J.,
1018 Johnson, G. C., Kaser, G., Kattsov, V., Kennedy, J., Klein Tank, A. M. G., Le Quere, C., Myhre,
1019 G., Osborn, T., Payne, A. J., Perlwitz, J., Power, S., Prather, M., Rintoul, S. R., Rogelj, J.,
1020 Rusticucci, M., Schulz, M., Sedlacek, J., Stott, P. A., Sutton, R., Thorne, P. W., and Wuebbles,
1021 D.: Climate Change 2013. The Physical Science Basis. Working Group I Contribution to the
1022 Fifth Assessment Report of the Intergovernmental Panel on Climate Change - Abstract for
1023 decision-makers; Changements climatiques 2013. Les elements scientifiques. Contribution du
1024 groupe de travail I au cinquieme rapport d'evaluation du groupe d'experts intergouvernemental
1025 sur l'evolution du CLIMAT - Resume a l'intention des decideurs, 2013.
- 1026 Strandberg, G., Kjellström, E., Poska, A., Wagner, S., Gaillard, M.-J., Trondman, A.-K., Mauri,
1027 A., Davis, B. a. S., Kaplan, J. O., Birks, H. J. B., Bjune, A. E., Fyfe, R., Giesecke, T., Kalnina,
1028 L., Kangur, M., van der Knaap, W. O., Kokfelt, U., Kuneš, P., Latal owa, M., Marquer, L.,
1029 Mazier, F., Nielsen, A. B., Smith, B., Seppä, H., and Sugita, S.: Regional climate model
1030 simulations for Europe at 6 and 0.2 k BP: sensitivity to changes in anthropogenic deforestation,
1031 *Climate of the Past*, 10, 661–680, <https://doi.org/10.5194/cp-10-661-2014>, 2014.
- 1032 Swann, A. L., Fung, I. Y., Levis, S., Bonan, G. B., and Doney, S. C.: Changes in Arctic
1033 vegetation amplify high-latitude warming through the greenhouse effect, *Proceedings of the*
1034 *National Academy of Sciences*, 107, 1295–1300, <https://doi.org/10.1073/pnas.0913846107>,
1035 2010.
- 1036 Thompson, A. J., Tabor, C. R., Poulsen, C. J., and Skinner, C. B.: Water isotopic constraints on
1037 the enhancement of the mid-Holocene West African monsoon, *Earth and Planetary Science*
1038 *Letters*, 554, 116677, <https://doi.org/10.1016/j.epsl.2020.116677>, 2021.
- 1039 Tian, Y., Woodcock, C. E., Wang, Y., Privette, J. L., Shabanov, N. V., Zhou, L., Zhang, Y.,
1040 Buermann, W., Dong, J., Veikkanen, B., Häme, T., Andersson, K., Ozdogan, M., Knyazikhin,
1041 Y., and Myneni, R. B.: Multiscale analysis and validation of the MODIS LAI product: I.
1042 Uncertainty assessment, *Remote Sensing of Environment*, 83, 414–430,
1043 [https://doi.org/10.1016/S0034-4257\(02\)00047-0](https://doi.org/10.1016/S0034-4257(02)00047-0), 2002a.
- 1044 Tian, Y., Woodcock, C. E., Wang, Y., Privette, J. L., Shabanov, N. V., Zhou, L., Zhang, Y.,
1045 Buermann, W., Dong, J., Veikkanen, B., Häme, T., Andersson, K., Ozdogan, M., Knyazikhin,
1046 Y., and Myneni, R. B.: Multiscale analysis and validation of the MODIS LAI product: II.
1047 Sampling strategy, *Remote Sensing of Environment*, 83, 431–441,
1048 [https://doi.org/10.1016/S0034-4257\(02\)00058-5](https://doi.org/10.1016/S0034-4257(02)00058-5), 2002b.
- 1049 Tierney, J. E., Pausata, F. S. R., and deMenocal, P. B.: Rainfall regimes of the Green Sahara,
1050 *Science Advances*, 3, e1601503, <https://doi.org/10.1126/sciadv.1601503>, 2017.



- 1051 Tiwari, S., Ramos, R. D., Pausata, F. S. R., LeGrande, A. N., Griffiths, M. L., Beltrami, H.,
1052 Wainer, I., de Vernal, A., Litchmore, D. T., Chandan, D., Peltier, W. R., and Tabor, C. R.: On
1053 the Remote Impacts of Mid-Holocene Saharan Vegetation on South American Hydroclimate: A
1054 Modeling Intercomparison, *Geophysical Research Letters*, 50, e2022GL101974,
1055 <https://doi.org/10.1029/2022GL101974>, 2023.
- 1056 Velasquez, P., Kaplan, J. O., Messmer, M., Ludwig, P., and Raible, C. C.: The role of land cover
1057 in the climate of glacial Europe, *Climate of the Past*, 17, 1161–1180, <https://doi.org/10.5194/cp-17-1161-2021>, 2021.
- 1059 Yang, W., Tan, B., Huang, D., Rautiainen, M., Shabanov, N. V., Wang, Y., Privette, J. L.,
1060 Huemmrich, K. F., Fensholt, R., Sandholt, I., Weiss, M., Ahl, D. E., Gower, S. T., Nemani, R.
1061 R., Knyazikhin, Y., and Myneni, R. B.: MODIS leaf area index products: from validation to
1062 algorithm improvement, *IEEE Transactions on Geoscience and Remote Sensing*, 44, 1885–1898,
1063 <https://doi.org/10.1109/TGRS.2006.871215>, 2006.
- 1064 Zeng, Z., Wang, D., Yang, L., Wu, J., Ziegler, A. D., Liu, M., Ciais, P., Searchinger, T. D.,
1065 Yang, Z.-L., Chen, D., Chen, A., Li, L. Z. X., Piao, S., Taylor, D., Cai, X., Pan, M., Peng, L.,
1066 Lin, P., Gower, D., Feng, Y., Zheng, C., Guan, K., Lian, X., Wang, T., Wang, L., Jeong, S.-J.,
1067 Wei, Z., Sheffield, J., Caylor, K., and Wood, E. F.: Deforestation-induced warming over tropical
1068 mountain regions regulated by elevation, *Nat. Geosci.*, 14, 23–29,
1069 <https://doi.org/10.1038/s41561-020-00666-0>, 2021.
- 1070